A General Method for Three Color STED Microscopy with One Depletion Laser: Application to Primary Neuronal Culture

by

Mackenzie C. Lee

B.S. Biomedical Sciences, B.A. German Studies
University of South Florida, 2016

Submitted to the Department of Brain and Cognitive Sciences
in Partial Fulfillment of the Requirements for the Degree of

Master of Science in Neuroscience
at the
Massachusetts Institute of Technology
May 2020

Signature of author: _____

Department of Brain and Cognitive Sciences
May 8, 2020

Certified and Accepted by: _____

Rebecca Saxe

John W. Jarve (1978) Professor in Brain and Cognitive Sciences

Associate Head, Department of Brain and Cognitive Sciences

Affiliate, McGovern Institute for Brain Science

Thesis Supervisor

A General Method for Three Color STED Microscopy with One Depletion Laser: Application to Primary Neuronal Culture

Mackenzie C. Lee

Submitted to the Department of Brain and Cognitive Sciences on May 8, 2020 in Partial Fulfillment of the Requirements for the Degree of Master of Science in Neuroscience

ABSTRACT

Recent advances in the field of optical nanoscopy have equipped molecular neuroscientists with the means to investigate sub-synaptic phenomena with unprecedented spatial resolution. Indeed, early studies employing these methodologies have revealed an extraordinary level of nanoscale spatiotemporal organization of complex and highly dynamic molecular architectures at the pre- and postsynaptic compartments. How exactly these supramolecular complexes are modified through time and experience, though, remains largely unknown. Moreover, the mechanisms by which pre- and postsynaptic protein organization specifies the biochemical and electrophysiological properties of a synapse have yet to be adequately described.

The purpose of the current study is thus to develop an inexpensive, accessible platform for super-resolution microscopy (SRM) of synaptic nanostructure. Though most SRM modalities are too technically and/or financially demanding for widespread use, basic stimulated emission depletion (STED) microscopy systems are now available to researchers at many institutions and require very little training to begin successfully acquiring SR images. One caveat, however, of many such systems is that they may only be capable of SR imaging in two spectral windows due to the inclusion of only one depletion laser in their design.

As SR imaging of only two proteins concurrently only promises limited insight into synaptic nanostructure, expansion of these systems' capabilities to localize even one more label would be highly advantageous in these experimental designs and model building. The present study thus develops and optimizes a method to obtain three color SR images on a microscope with a single STED beam. The unique spectral properties of a long Stokes shift dye, ATTO 490LS, are exploited to add another SR-capable channel without any instrument modifications. This protocol is then applied to image four synaptic proteins simultaneously in primary neuronal culture, with three imaged at STED resolution. More specifically, a tyrosine-phosphorylated subpopulation of the GluA2 glutamate receptor subunit is localized alongside the postsynaptic scaffolding proteins PSD-95 and PSD-93 with the pre-synaptic protein Munc-13 as a confocal landmark. The superior spatial resolutions achieved in this study establish this protocol as an accessible and robust method to introduce an extra SR channel into existing 2-color STED imaging paradigms.

TABLE OF CONTENTS

REVIEW OF LITERATURE

MOLECULAR BIOLOGY OF THE SYNAPSE

When Santiago Ramón y Cajal first proposed the neuron doctrine in 1888, that the nervous system is composed of a network of finite, distinguishable units, the theory implied that evolution had solved a unique engineering problem in neuronal communication. Namely, the electrical impulses with which neurons communicate must somehow traverse a ~20-40 nanometer gap between adjacent neurons. In the time since, researchers have generated an impressive reservoir of knowledge regarding how synapses, the sites of contact between two neurons, convert electrical into chemical signals so that information flows seamlessly between neurons.

In neuronal signaling, when a membrane depolarization event triggers an action potential in a neuron, this electrical signal travels from the axon initial segment adjacent to the cell body along the axon until it reaches a specialized membrane structure called the presynaptic active zone. As the action potential reaches the active zone, membrane depolarization drives voltage-gated calcium channels bound in a vesicle release complex by the RIM family of scaffolding proteins to open. The resultant regional calcium influx activates calcium-sensitive synaptotagmin-1 protein to trigger the binding and rearrangement of vesicle- and membrane-bound SNARE tethering proteins. The mechanical tension effected by these complexes then fuses the bound vesicles to the membrane, opening a fusion pore through which contained neurotransmitters enter the synaptic cleft. From membrane depolarization to neurotransmitter release, this entire process occurs in the span of a few hundred microseconds (Südhof, 2012; Südhof, 2013).

These neurotransmitters then diffuse across the synaptic cleft and bind to glutamatergic receptors on the postsynaptic side. Glutamate binding to α-amino-3-hydroxy-5-methyl-4-isoxazolepropionic receptors (AMPARs), the primary mechanism of fast excitatory neurotransmission, induces pore opening at the center of the receptors, through which sodium and other monovalent cations pass to trigger postsynaptic membrane depolarization. This core postsynaptic machinery, however, is nested within an extensive network of at least ~460 other

proteins involved in at least 13 different cellular functions, including cytoskeletal dynamics, kinase and GTPase signaling cascades, cell adhesion, and receptor function, among others (Peng *et al*., 2004; Collins *et al*., 2006; Sheng and Kim, 2011).

Primary among these protein families are the ionotropic glutamatergic receptors that conduct ion currents in response to glutamate binding: AMPARs, composed of GluA subunits; N-methyl-D-aspartate receptors (NMDARs; GluN subunits); and kainate receptors (KARs). Each receptor exists as a tetramer, with preferred combinations conferring specific biophysical properties onto the channel corresponding to its main functions. For example, NMDARs display slow activation and desensitization kinetics on the order of tens and hundreds of milliseconds, respectively; require postsynaptic depolarization to remove a Mg^{2+} channel block; conduct calcium; and are highly sensitive to glutamate, with EC_{50}'s in the sub-micromolar range. AMPARs, conversely, display rapid, sub-millisecond activation and millisecond desensitization kinetics; typically only conduct monovalent cations; and are only sensitive to higher concentrations of glutamate, in the high micromolar to millimolar range. Sustained activation of NMDARs in response to successful synaptic communication across an extended dynamic range thus effects long-lasting currents capable of triggering calcium-sensitive signaling cascades. In contrast, AMPARs rapidly respond to strong pulses of pre-synaptic activity with larger conductances whose principal purpose is to trigger post-synaptic membrane depolarization for electrical signal relay (Mayer *et al*., 1984; Traynelis *et al*., 2010; Paoletti *et al*., 2013; Reiner and Levitz, 2018).

In addition to variations in AMPAR subunit composition, the receptors interact with two families of auxiliary subunits, Transmembrane AMPAR Regulatory Proteins (TARPs; Tomita *et al*., 2003) and the cornichon-like proteins CNIH2/CNIH3 (Schwenk *et al*., 2009). These proteins function as primary modulators of AMPAR function: they can stabilize AMPAR protein and surface expression levels; slow decay, deactivation, and desensitization kinetics; modulate AMPAR subunit composition; and anchor the receptors to postsynaptic scaffolding molecules, among other roles (Straub and Tomita, 2012). AMPA receptors are also subject to various post-translational modification. GluA2, for example, can be ubiquitinated at K870/K882 (Widargdo, *et al*., 2015; Widargdo *et al*., 2017); palmitoylated at C836 (Hayashi *et al*., 2005); O-GlcNAcylated (Taylor *et*

al., 2014); and phosphorylated at S863/S880 by Protein Kinase C, S588 by Casein Kinase II, and Y876 by Src family tyrosine kinases (Chung *et al*., 2000; Hayashi and Huganir, 2004; Lussier *et al*., 2015; Diering and Huganir, 2018).

Supporting these key postsynaptic membrane proteins is a dense mesh of scaffolding proteins forming a protein-rich region called the postsynaptic density (PSD). Chief among the scaffolding proteins are members of the membrane-associated guanylate kinase (MAGUK) family of proteins, including PSD-95, PSD-93, SAP102, and SAP97. MAGUK family proteins are critical to the integrity of the postsynaptic signaling apparatus. Knockdown of PSD-95 alone already triggers dramatic structural reorganization of the PSD and functional deterioration (Chen *et al.*, 2011). Further elimination of PSD-93 and SAP102 leads to profound impairment of synaptic function, reduction in the size of PSDs, and loss of AMPA and NMDA receptors from the synaptic cleft (Chen *et al*., 2015). MAGUKs thus function as master organizers of the postsynaptic density, performing roles as varied as AMPA and NMDA receptor trafficking (Elias *et al*., 2006; Lau *et al*., 2007; Chen *et al*., 2012; Levy *et al*., 2015), recruitment of intracellular signaling enzymes (Won *et al.*, 2016), and refinement of trans-synaptic alignment through its interactions with adhesion molecules (Irie *et al*., 1997), among others (reviewed in Sheng and Kim, 2011; Won *et al*., 2017). In accordance with this surfeit of evidence for the importance of supramolecular scaffolds, questions regarding exactly which postsynaptic proteins form complexes with MAGUK scaffolds, the heterogeneity of these complexes across the PSD, and the signaling cascades that affect complex composition have become highly active areas of investigation in recent years.

FLUORESCENCE NANOSCOPY

Given the (1) ubiquity of supramolecular protein complexes at the synaptic cleft, (2) their interactions with dynamic scaffolding molecules, and (3) the consequent nanometer precision of protein activity and neurotransmitter gradients in synaptic transmission, experimental techniques with molecular specificity and resolution are necessary to establish a viable model for molecular architecture and dynamics at the synapse. Methods in biochemistry and molecular biology, however, suffer from the averaging effects of bulk sample preparation and detection,

such that the various contributing subpopulations and spatiotemporal profiles of synaptic proteins are rendered unresolvable. Fortunately, new molecular and optical technologies in fluorescence microscopy around the turn of the 21st century prompted the widespread adoption of this technique in the biological sciences for exactly this purpose, i.e. to elucidate the spatiotemporal constraints of cellular signaling and organization with molecular specificity (reviewed in Sahl *et al.*, 2017; Sigal *et al.*, 2018). Despite these advances, the synaptic phenomena above would still present a unique technical challenge: their nanoscale dynamics and architecture operate well below a fundamental physical limit to the resolving capacity of a light microscope.

The resolution of an optical system is defined as the minimum distance required between two objects such that they can be discerned reliably as two separate objects. In fluorescence microscopes, the optical path focuses light at the sample plane, where it excites fluorophores on the sample, which in turn emit light back through the optical path to the camera or detector. Due to the wave nature of light, however, the incident light does not focus to an infinitely small point as it approaches the sample. Instead, the phenomenon of diffraction, in which propagating waves do not travel uniformly in one direction but rather deflect radially from each point along the wave-front, causes the light to blur as it reaches the sample plane. The converging light waves fill and excite a shaped volume known as an Airy disk at the focal point, with their intensity profiles convolved across space according to an impulse response called the point spread function (PSF). The consequence of these optical phenomena for the resolving ability of a microscope is defined by Abbe's diffraction limit, which restricts the maximum resolution of any optical system to about half of the wavelength of its illumination source (Abbe 1873). This sets the lower bounds of distances resolvable by conventional fluorescence microscopy at about 200 nanometers.

The problem of resolution in light microscopy presents itself thus: it is impossible to discern how many and which molecules within the Airy disk volume are fluorescing. The solution that various modes of "super-resolution" microscopy (SRM), or nanoscopy, have since proposed and implemented is to exploit "on" and "off" molecular states of the fluorophores, such that only a limited subset are fluorescent-competent at any given point. Since the first proposal to use molecular state transitions to design diffraction-unlimited microscopy methods in 1994 (Hell and

Wichmann), two major design concepts and numerous variations thereof have dominated the field of nanoscopy. Coordinate-targeted methods (**Figure 1A**) employ torus, or "donut", shaped wave-fronts to shutter molecular states within the diffraction-limited confocal volume of a raster-scanning microscope (Hell and Wichmann, 1994; Hell and Kroug, 1995; Hofmann *et al*., 2005; Balzarotti *et al.*, 2016; Danzl *et al*, 2016). Coordinate-stochastic, or pointillist, methods (**Figure 1B**) utilize probabilistic molecular transitions across time to mathematically reconstruct SR images from a series of diffraction-limited widefield images (Dickson *et al*., 1997; Betzig *et al*., 2006; Hess *et al*., 2006; Rust *et al.*, 2006; Sharanov *et al.*, 2006; Bates *et al.*, 2007; Fölling *et al*., 2008). A third commonly used SR design is a variation of the diffraction-limited method structured illumination microscopy (SIM; **Figure 1C**). SIM and its variations use a series of periodic illumination patterns to shift high frequency (i.e. resolution) information in the image into lower frequency Fourier space, making it available to the microscope as moiré fringes, from which an image with about twofold improved resolution can be mathematically reconstructed (Gustaffson, 2000). Saturated SIM (SSIM) generates diffraction-unlimited images by combining periodic illumination patterns with fluorescence nonlinearities that produce higher frequency harmonics across the frequency domain (Gustaffson, 2005). Various other SR methods do exist, though they are less frequently used and often require extensive experience in instrument design and operation (reviewed in Hell, 2009; Hell *et al.*, 2015; Sydor *et al.*, 2015; Sahl *et al.*, 2017; Sigal, *et al.*, 2018; Schermelleh *et al.*, 2019).

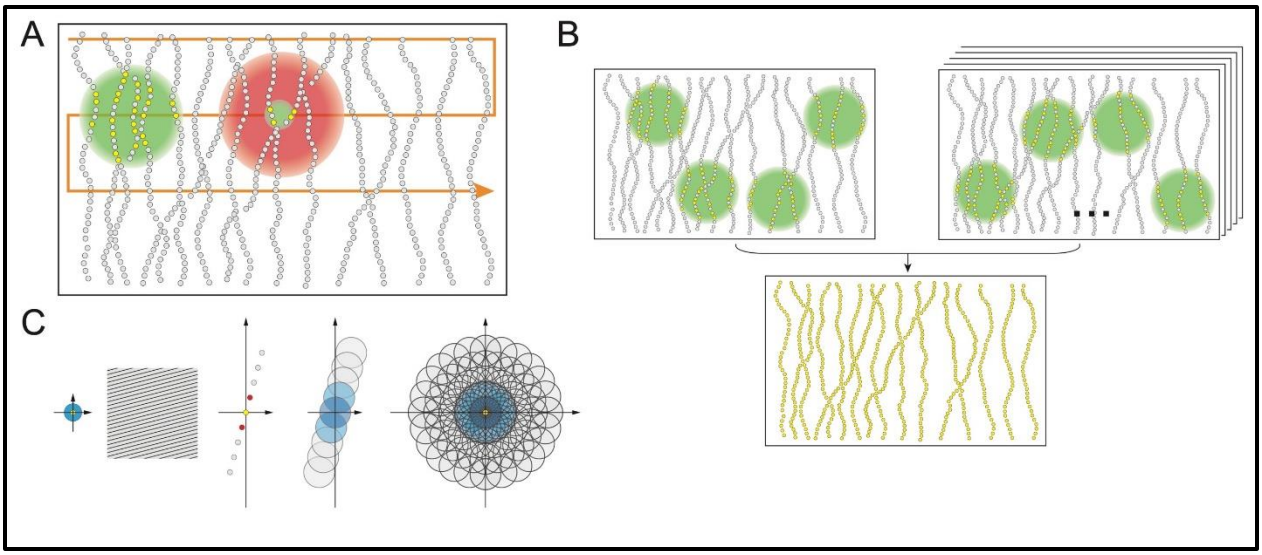

Figure 1. Major design paradigms in super-resolution microscopy. SR microscopy depends on on-off fluorescence state transitions. **A** Coordinate-targeted techniques like STED and RESOLFT use beam shaping to generate donut shaped lasers that modulate on-off states surrounding the scan locus. **B** Coordinate-stochastic/pointillist approaches employ stochastic transitions in fluorescent state across many acquisitions to reconstruct SR images computationally. **C** Structured illumination approaches improve resolution by calculating interference (moiré) fringes generated by non-uniform illumination of the sample. These fringes shift high resolution features to lower frequency spaces in the Fourier domain.

Of the coordinate-targeted approaches, the oldest and most widely used is stimulated emission depletion (STED) microscopy (reviewed in Vicidomini *et al.*, 2018). This approach takes advantage of a particular photophysical phenomenon called stimulated emission, first posited by Einstein in the early 20th century (Einstein, 1916; Einstein, 1917). A thorough understanding of this process, however, requires an understanding of basic fluorophore photophysics. When a fluorophore absorbs a photon (on the femtosecond timescale), an electron in the fluorophore will be excited from the ground state (S_0) to an excited state (e.g. S_1 or S_2; **Figure 2**). After non-radiative vibrational relaxation of the fluorophore (picoseconds), the fluorophore will fluoresce (nano- to picoseconds; a form of radiative relaxation) and release a photon with a wavelength defined by the energy transition of the electron during relaxation.

This stochastic process can be quantitatively defined in both energy and time. The energy transitions are inherent characteristics of the fluorophore's chemistry and are reflected in its fluorescence *excitation and emission spectra*. The time that this process takes is defined as the

fluorescence lifetime (τ), which describes the exponential probability distribution of the likelihood of photon emission across time (**Figure 3B**).

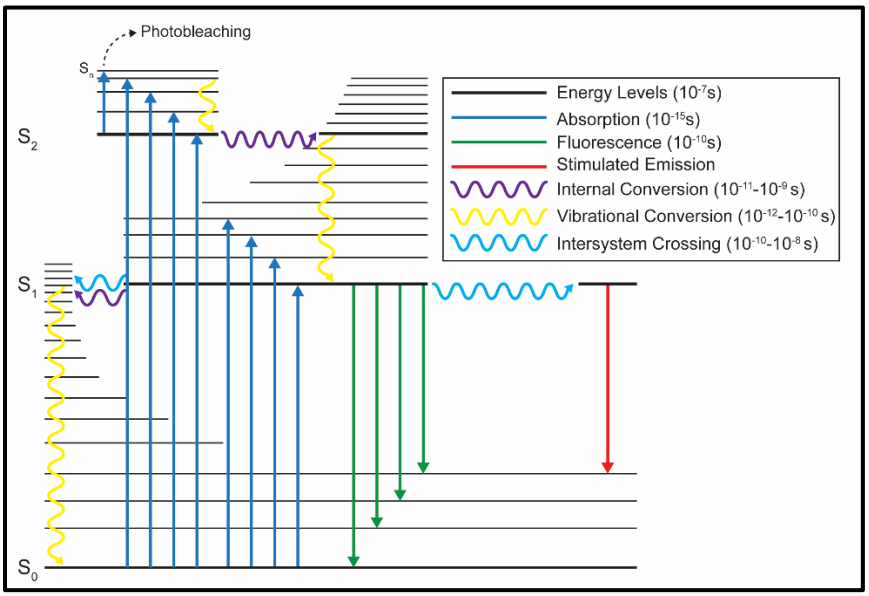

Figure 2. The photophysics of fluorescence and stimulated emission. When a fluorophore absorbs a photon, an electron is excited from the ground state (S_0) to an excited state (S_1 and higher). Various intramolecular rearrangements can follow, each at different timescales. The fluorophore emits a photon when the electron undergoes radiative decay back down to the ground state. Stimulated emission interferes with this process and forces the electron to a lower energy level before spontaneous decay can occur.

The process of stimulated emission as used in STED microscopy bypasses the spontaneous radiative decay process of normal fluorescence and forces the excited fluorophore electron to decay via an alternative mechanism. It does so by striking the fluorophore with another photon with a wavelength that corresponds exactly to the energy difference between ground (S_0) and excited states (S_1). The excited electron then decays, emitting a photon with the same direction, wavelength, phase, and polarization as the stimulating photon (Vicidomini *et al*., 2018).

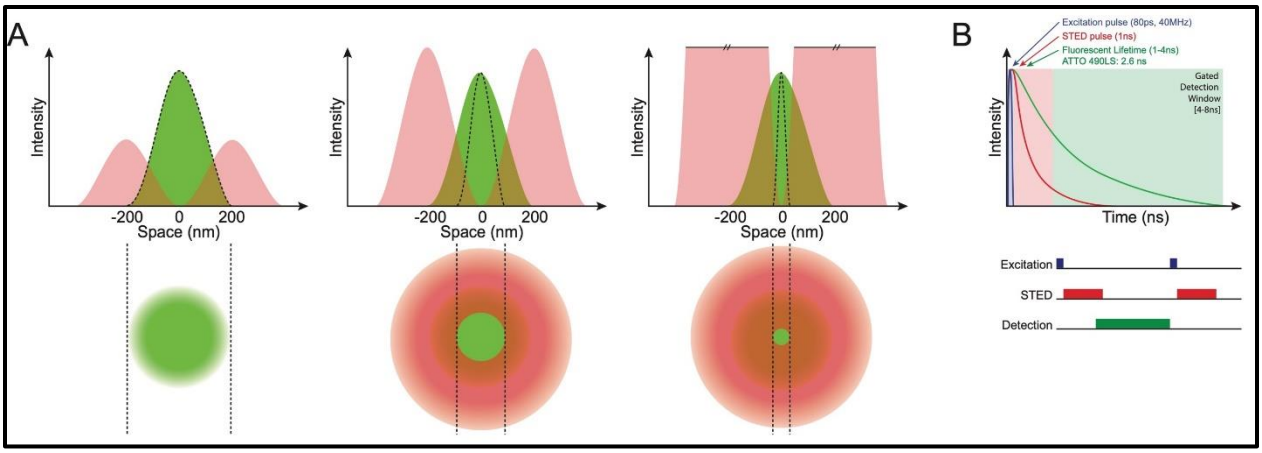

Figure 3. Resolution scaling and gating in STED microscopy. A The intensity of the depletion beam, depicted here as the integral of the area illuminated by the donut, correlates directly with the area of the sample emitting light, and thus the achievable resolution of the system. **B** Gated STED involves the calibration of the laser pulse sequence and detector gating to the fluorescence lifetime of the fluorophore. The 1 ns STED pulse is applied immediately after a brief excitation pulse. The effective fluorescent lifetime of affected fluorophores (red line) is dramatically reduced, such that most fluorescence emission occurs prior to the detector's gating. Unaffected fluorophores (green line) still emit with normal kinetics, such that these two signals can be differentiated with the selective detection window.

Stimulated emission is thus exploited in STED microscopy as the means to force a targeted subpopulation of fluorophores into the "off" state. In this approach, a Laguerre-Gaussian depletion beam, shaped by either a spiral phase plate or spatial light modulator (SLM), illuminates a toroidal cross-section of the sample plane, forcing fluorophores within its volume to de-excite through stimulated emission. The "donut" beam features an intensity minimum at its center, where fluorophores do not receive enough of its energy to "turn off" (**Figure 3A**). This effectively restricts the population of fluorophores within the diffraction-limited Airy disk that can spontaneously fluoresce, whose fluorescence is then detected and registered to the current coordinates of the raster-scanning confocal microscope (hence, coordinate-targeted SRM). Importantly, the spatial resolution achievable by a STED microscope scales with the intensity of the STED beam. As the intensity of the depletion beam increases, the area of the excitation volume that receives enough energy to emit via stimulated emission decreases exponentially, leading to an ever-smaller effective PSF. For this reason, STED is considered diffraction-unlimited, in that it can theoretically achieve infinite spatial resolution, though in practice its resolution is limited to the tens of nanometers range by the photophysics of available fluorophores.

The variant of STED most widely used in commercial STED systems is called gated-STED, or g-STED, to distinguish it from continuous wave (CW)-STED (Vicidomini *et al.*, 2011). Whereas the latter uses continuous wavelength excitation and depletion lasers, g-STED employs ultrashort pulsed excitation and STED lasers with gated detectors to improve the signal-to-noise ratio (SNR) and effective spatial resolution of measurements (**Figure 3B**). Briefly, following an ~80 picosecond (i.e. 10^{-15} second) excitation pulse, a 1 ns depletion pulse de-excites the fluorophores in the STED donut's volume before most of them can relax through spontaneous emission, which takes much longer (~2-5 ns). The detector then shutters open for a brief period to collect the photons from the reduced excitation volume. This has two effects: (1) photons from the depletion region that fluoresce before being affected by the STED beam are not collected, and (2) long-wavelength photons from stimulated emission cannot produce crosstalk in far-red channels. Both of these improve the SNR of the microscope and, in doing so, extend the spatial resolutions it can achieve.

FLUORESCENCE NANOSCOPY IN NEUROSCIENCE

These advances in fluorescence microscopy have since been widely accepted by the neuroscience community as solutions to the restrictions the diffraction limit had previously imposed upon research into neuronal biology. Indeed, the first application of SR microscopy to a biological problem utilized STED microscopy to investigate synaptotagmin dynamics within the presynaptic active zone (Willig *et al.* 2006). This has now been followed by over a decade of fruitful insights into neuronal function with SR microscopy.

Of these studies, the most prominent lines of inquiry can be roughly divided into two topic areas: (1) cytoskeletal and (2) synaptic nanostructure and dynamics. With regard to the former, in 2013, Xu and colleagues first described a ~190-nm periodic ring-like scaffold composed of adducin-capped actin interspersed with spectrin tetramers spanning the diameter of axons (Xu *et al.* 2013; Leterrier *et al*., 2015; Leite *et al.*, 2016). This structure has since also been found in dendrites (Zhong *et al*., 2014; D'Este *et al.*, 2015), spine necks (Bär et al., 2015; Sidenstein et al., 2015), and even nodes of Ranvier (D'Este *et al.*, 2017) across a multitude of neuron types (D'Este *et al.*,

2016; He *et al*., 2016) and glia (Lukinavicius *et al.*, 2014). More proteins were also found to reside in the structure, from adhesion molecules, to ion channels, to ankyrins, among others. Moreover, the scaffold appears to function beyond its role in structural integrity: the lateral diffusion of axon initial segment membrane proteins is confined with the ~190-nm segments, indicating that these structures are instrumental in establishing functional microdomains throughout the neuronal membrane (Albrecht *et al.* 2016). Beyond this extensive literature on cytoskeletal periodicity, nanoscopy has also been applied repeatedly to the study of live dendritic spine dynamics (Nägerl *et al.*, 2008; Testa *et al*., 2012; Chazeau *et al*., 2014; Takasaki and Sabatini, 2014; Tonneson *et al*., 2014; Urban *et al.*, 2018) and how they correlate with long-term potentiation (Bosch *et al.*, 2014).

Synaptic nanostructure has been a persistent topic of interest to the SR imaging community ever since SRM's first applications to biological questions (Kittel *et al.*, 2006; Willig *et al*., 2006). In the years since, every subregion of the synapse has been scrutinized with SR imaging across a number of organisms and neuron types. Many of the first explorations of subsynaptic structure focused on the release machinery of the active zone at *Drosophila* neuromuscular junctions, revealing mechanisms of maturation, neurotransmitter release, and vesicular organization (Fouquet, *et al*., 2009; Owald *et al*., 2010; Liu *et al.*, 2011; Ehmann *et al*., 2014; reviewed in Ehmann *et al*., 2015). Subsequent experiments on presynaptic organization have demonstrated mechanistic links between presynaptic nanostructure and synapse electrophysiological properties (Glebov *et al.*, 2017; Fulterer *et al*., 2018; Sakamoto *et al*., 2018) and explored the role of (nano)modularity in active zone dynamics during plasticity processes (Böhme *et al*., 2019; Goel *et al*., 2019). One landmark study combined mass spectrometry, electron microscopy, and SR light microscopy to generate a three-dimensional model of the average synaptic bouton, cataloguing and localizing thousands of proteins in the process (Wilhelm *et al*., 2014).

Though SR studies of postsynaptic nanostructure trailed presynaptic studies by a number of years, they have now generated a wealth of information connecting postsynaptic structure to function and dynamics. Many have focused on mechanisms through which AMPA receptor clustering and organization underlie and reinforce efficient neurotransmission (Hoze *et al*., 2012; MacGillavry, *et al.*, 2013), and how intracellular signaling can modulate these features (Fukata *et al.*, 2013). Other investigations have explored PSD-95's role in AMPAR trafficking and positioning

at the synapse and the plasticity of these nanodomains during synaptic remodeling (Nair *et al*., 2013; Broadhead *et al.*, 2016; Hruska *et al.*, 2018). Two recent studies even extended these explorations to *in vivo* systems monitoring PSD-95 structural stability and morphology over time in living mouse brains with STED microscopy (Masch *et al*., 2018; Wegner *et al*., 2018). Other studies have also branched out from PSD-95 and AMPAR dynamics at excitatory synapses, characterizing the nanoscale topography of NMDA receptors at the PSD (Kellermayer *et al*., 2018) and the subsynaptic nanomodules of inhibitory synapses (Crosby *et al*., 2019).

Lastly, a substantial body of work has advanced towards the goal of a more holistic understanding of synaptic nanodomains and the role the play in coordinating pre- and postsynaptic activities. This research has revealed extraordinary spatial precision in pre-/postsynaptic interactions (Dani *et al*., 2010; Nishimune *et al*., 2016) and explored how trans-synaptic adhesion molecules like neurexin-1 may fine tune and modify these interactions. One particularly influential study has even proposed the existence of trans-synaptic "nanocolumns" that align neurotransmitter release and detection machineries for maximally effective neurotransmission (Tang *et al*., 2016). Therefore, though this science and these techniques are only now maturing, the earliest applications of SRM in the study of synaptic nanostructure, its molecular features, and dynamics predict a critical role of these investigations in our efforts to demystify synaptic function.

STUDY DESIGN

The exciting neurobiological insights engendered by new methods in nanoscopy point to a general utility of SR imaging techniques in the molecular neuroscience laboratory. Several challenges, however, continue to hinder its widespread adoption in the field. First, coordinate-stochastic and advanced structured illumination methods require considerable expertise in the physical principles and/or computational methods used in post-hoc processing. Both designs are prone to artifacts in inexperienced hands, such that an expert collaborator is typically needed to safeguard possible analysis errors. Secondly, most commercial SR imaging platforms are prohibitively expensive for the individual investigator, particularly when the microscope is inaccessible to novices and will require considerable training before its successful application to the laboratory's research questions. Accordingly, most SR microscopes are only available to investigators as shared facility resources. Lastly, nanoscopy experiments often demand time- and resource-intensive optimization before data can even start to be collected.

For these reasons, great effort has been applied in recent years to commercialize SR microscopes in accessible formats. Of these, modern commercial STED microscopes are particularly notable as promising options to the novice SR microscopist. The operation of a STED microscope is largely identical to a standard confocal microscope with only the addition of the depletion laser and detector gating. Though beginners may have difficulty achieving state-of-the-art spatial resolution immediately, it is more than likely that they will achieve some resolution improvement. Importantly, STED microscopy is also less prone to artifacts than other SR modalities, and of those that do occur, most are false negative results due to oversaturation with the depletion beam, as opposed to the false positive results more common in other methods (e.g. periodic artifacts in SIM imaging). Lastly, neither post-hoc computational processing nor knowledge of the physical principles of STED are necessary in imaging.

One current limitation of affordable commercial STED systems, however, is that many only boast one STED laser at 775 nm. As a consequence, these microscopes can only provide diffraction-unlimited resolution of the two labels in the red and far-red channels using standard imaging methods. One such example is the STEDYCON super-resolution scanning module sold by Abberior

Instruments, Inc. This system can be used to convert a standard epifluorescent microscope into a multicolor confocal scanning STED system at a fraction of the cost of a full STED microscope system (see **Methods** for further specifications). All implementations of the STEDYCON to date, though, have only included a single 775 nm STED beam, and their routine use is thus limited to two color SR imaging experiments.

Several recent studies, however, have implemented novel dye chemistry to achieve three color STED imaging with only one depletion laser (Sidenstein *et al*., 2016; Butkevich *et al.*, 2017; reviewed in Sednev *et al*., 2015). In these works, dyes with exceptionally long Stokes shifts, i.e. spectral displacement between their excitation and emission peaks, were employed to allow one other excitation laser line to image at STED resolution. In short, an extra pulsed excitation laser blue-shifted from the main STED channels is used to excite a long Stokes shift (LSS) dye. The emission spectrum of the LSS dye overlaps with the STED beam (cf. **Figure 4B**), so it can be depleted efficiently to generate a super-resolution image. As such, a third SR channel can be added to the microscope design by using a fluorophore that emits much farther from its excitation wavelength than a normal dye and is thereby within range of the STED effect.

Inclusion of a third SR channel in microscope setups has clear advantages to the study of synaptic nanostructure, for much more detailed models become possible when the relative positions of three proteins can be precisely determined with diffraction-unlimited resolution. Namely, three coordinates across a 2D imaging plane permit reconstruction of the relative position of as many synaptic proteins as desired by cross-referencing shared labels between experiments. A further confocal reference channel, also implemented in this study, can be used to orient postsynaptic protein complexes to the presynaptic active zone. The purpose of this project was thus to develop and optimize a general protocol for three color super-resolution imaging with a confocal reference using the STEDYCON system that requires no further expertise from users beyond a working knowledge of STED imaging with this microscope.

To demonstrate the utility of such a protocol for studies of synaptic nanostructure, the final protocol was applied to samples for study of the localization of PSD-93, PSD-95, GluA2, and tyrosine-phosphorylated (pY-) GluA2 (Y869/873/876). An abundance of previous work points to

a vital role for GluA2-containing AMPARs in tuning synaptic properties. For example, GluA2 has been found to be required for various forms of synaptic molecular rearrangements involved in plasticity processes, including long-term potentiation (LTP), long-term depression (LTD), and homeostatic synaptic scaling. GluA2-containing receptors mediate hippocampal LTP (Adesnik and Nicoll, 2007); NMDAR-dependent LTD (Zhou et al., 2018); cerebellar LTD (Chung et al., 2000; Steinberg et al., 2006); and bi-directional homeostatic plasticity (Gainey, et al., 2009; Ancona-Esselman et al., 2017; Diering et al., 2014; Tan et al., 2015; Tatavarty et al., 2013). Its involvement in these processes is primarily coordinated by modulation of its association with binding partners GRIP1/GRIP2 and PICK as a result of phosphorylation cycles driven by Src family kinases, Protein Kinase C, and Casein kinase II as well as PP1, STEP61, and PTPMEG phosphatases. These actions, in turn, affect AMPAR surface diffusion and trafficking to influence synaptic strength and tuning (Diering and Huganir, 2018).

With regard to phosphorylation cycles, the tyrosine phosphatase STEP61 has been recently demonstrated to be required for NMDAR removal from the PSD (Goebel-Goody *et al*., 2012). This action is antagonized by PSD-95-mediated STEP61 degradation, resulting in receptor stabilization (Won *et al.*, 2016). Similarly, PSD-95, along with SAP102, also recruits Fyn and Pyk2 tyrosine kinases to NMDA receptor complexes (Tezuka, *et al*., 1999; Seabold *et al.* 2003). Whether MAGUK family scaffolding proteins regulate AMPAR tyrosine phosphorylation (Hayashi and Huganir, 2004), however, remains unexplored. Moreover, the extent to which reported AMPAR tyrosine phosphorylation sites modulate AMPAR association with MAGUKs and TARP auxiliary subunits, in turn tuning GluA2-dependent synaptic properties, is completely unknown.

The present study thus explores a means to investigate the differential distribution and clustering of the MAGUKs PSD-93 and PSD-95 with pY-GluA2 (Y869/873/876) versus non-modified GluA2. An optimized three-color STED imaging protocol provides such a method, which can later be applied to murine tissue imaging of experimental specimens to evaluate the requirement of MAGUKs and/or experience-dependent plasticity in these processes. The result should then be easily accessible to novice STED microscopists to facilitate further investigations of the role of synaptic nanostructure in synaptic transmission in health and disease.

METHODS

MATERIALS

Primary Antibodies		
Antigen	**Source**	**Optimized Dilution**
PSD-93 (N18/30)	Neuromab	1:100
PSD-93	Synaptic Systems	1:100
PSD-95 (K28/43)	Neuromab	1:100
PSD-95 (K28/74)	Neuromab	1:100
GluA2	Alomone Labs	1:500
GluA2 (L21/32)	Abcam	1:500
pY-GluA2 (Y869/873/876)	Cell Signaling	1:500
Munc-13-1	Synaptic Systems	1:200
Mountant		
Item	**Catalog Number**	**Source**
ProLong™ Glass Antifade Mountant	P36982	ThermoFisher
Dye Conjugation		
Item	**Catalog Number**	**Source**
Atto490LS NHS ester	AD 490LS-31	ATTO-TEC
Sephadex G-25 in PD-10 Desalting Columns	17085101	GE Healthcare
NH2OH · HCl ReagentPlus 99%	159417	Millipore Sigma
Dimethyl Sulfoxide for Molecular Biology	D8418	Millipore Sigma

Table 1. Consumable Reagents. List of reagents used for staining (antibodies and mountant) and dye conjugation protocols.

MICROSCOPE SPECIFICATIONS

For all imaging, a second-generation STEDYCON confocal and STED module from Abberior Instruments, Inc., was affixed to the camera port of a standard upright epifluorescence microscope. Further specifications of the microscope are listed below in Table 2.

Excitation Lasers	488 nm (pulsed); 595 nm (pulsed); 640 nm (pulsed)
STED Laser	775 nm (pulsed)
Detectors	Time-gated APDs with (1) a dual BPF at 525±25 nm and 617.5±7.5 nm or (2) BPF at 675±25 nm
Scanner	QUAD beam scanner: 90µm x 80µm (with a 100x objective); 512x512 pixel up to 1.1 frames/s; line frequency up to 800Hz
Objective	100X, NA 1.4, piezoelectric focusing system

Table 2. Microscope Specifications. Relevant specifications for confocal and STED image acquisition with the STEDYCON. APD = avalanche photodiode (detector); BPF = bandpass filter.

CHOICE OF DYES AND EXCITATION/EMISSION PATHS

To perform multicolor imaging, it is necessary to plan and test options for dye use in conjugation with different excitation/emission paths. Important considerations in these choices include (1) the excitation efficiency of a laser for a corresponding fluorophore choice, as determined from the fluorophore's excitation spectrum and the laser's wavelength; (2) spectral separation of excitation and emission spectra of chosen fluorophores for minimal crosstalk; and (3) the collection efficiency of a detector for any given fluorophore, as determined by its emission spectrum in combination with the detector specifications.

For this protocol, a combination of fluorophores with green, red, and far-red emission spectra was chosen. The **green** fluorophore used in the confocal reference channel was AlexaFluor 488; suitable alternatives include Oregon Green, DyLight 488, ATTO 488, Chromeo 488, and Abberior Star 488, among others. The **red** fluorophore used for 775 nm STED imaging was AlexaFluor 594; commonly used alternatives include ATTO 590 and Abberior Star 580. The **far-red** fluorophore used for 775 nm STED imaging was Abberior STAR RED; suitable alternatives include ATTO 647N

and Janelia Fluor 646, among others. The **red long Stokes shift** dye used for 775 nm STED imaging was ATTO 490LS, Abberior Star 480 SXP, DyLight 485-LS, and Chromeo 494, among others. The laser lines used to excite the green, red, far-red, and long Stokes shift red dyes were the 488 nm, 595 nm, 640 nm, and 595 nm STEDYCON lasers, respectively.

A general schematic for excitation and emission spectra of the fluorophores used in this study can be found in **Figure 4A** and **4B**, respectively (schematic from *FPBase.org*; Lambert, 2019). Laser lines are included in **Figure 4A** for comparison with the fluorophores' excitation spectra as a measure of excitation efficiency. Likewise, the location and width of each filter are indicated in **Figure 4B** as determinants of the collection efficiency of each detector for any given fluorophore. Note that the left two detectors in 4B belong to the same detector, i.e. the avalanche photodiode detector (APD) with a 525±25 nm /617.5±7.5 nm dual bandpass filter (dual-BPF).

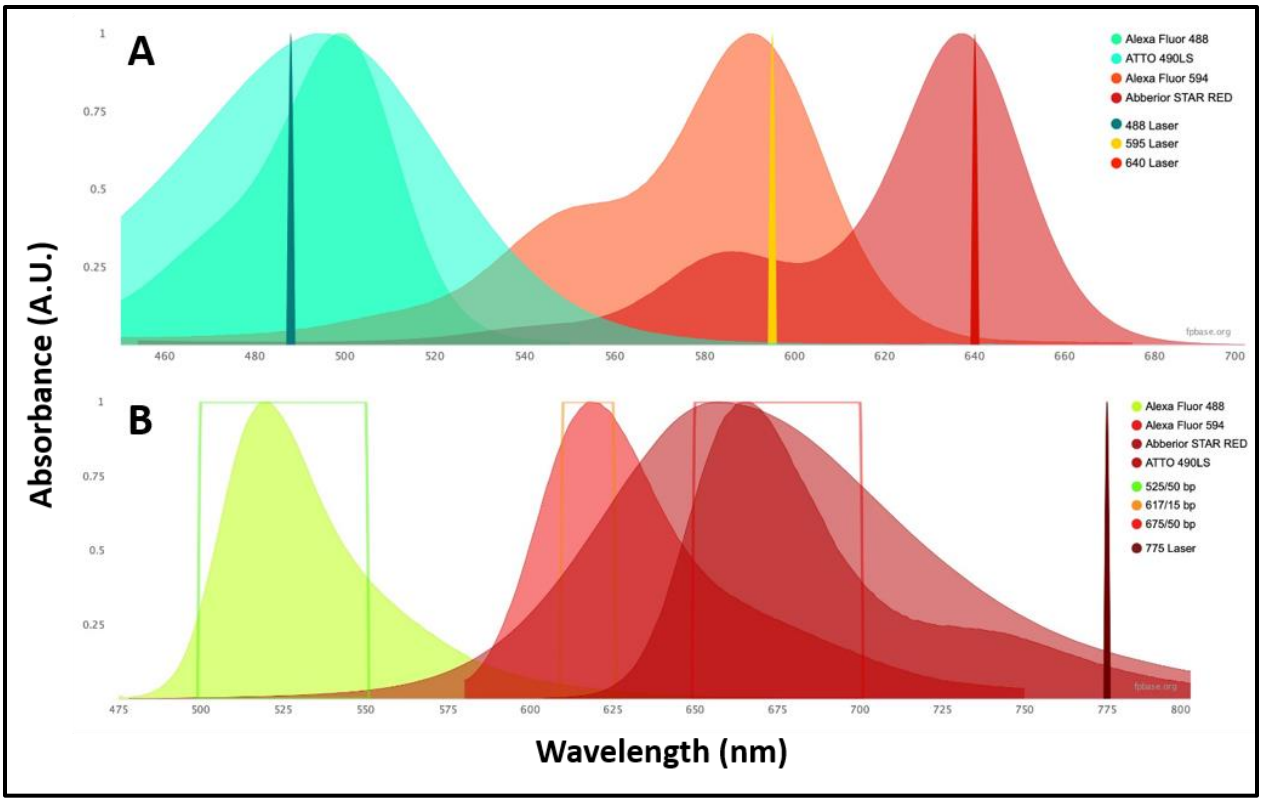

Figure 4. Fluorophore Spectra and the Microscope. A. Excitation spectra (normalized to maximum absorption) of the four fluorophores used in the study alongside the microscope's excitation laser wavelengths. **B.** Emission spectra (normalized to max) of each fluorophore alongside the STEDYCON emission filters and STED laser (775 nm). Note the extended width of the excitation and emission curves for ATTO 490LS. Figures from *FPBase.org* fluorophore spectra viewer with minor modifications (Lambert, 2019).

As **Figure 4A** demonstrates, the 488 nm laser strongly excites both Alexa Fluor 488 and ATTO 490LS dyes, the 595 nm laser effectively excites Alexa Fluor 594, and the 640 nm laser optimally excites Abberior STAR RED. **Figure 4B** indicates that the APD with a 525±25 nm/617.5±7.5 nm dual-BPF best captures emitted photons from Alexa Fluor 488 and Alexa Fluor 594. The APD with a 675±25 nm BPF likewise collects the most photons from ATTO 490LS and Abberior STAR RED.

It is thus salient that AlexaFluor488 would be best excited by the 488 nm laser and detected by APD1 (525±25 nm/617.5±7.5 nm dual-BPF); Alexa Fluor 594 excited by the 595 nm laser and detected with APD1; and Abberior STAR RED excited by the 640 nm laser and detected with APD2 (i.e. 675±25 nm BPF). The implementation of the long Stokes shift dye (i.e. ATTO 490LS), though, demands additional considerations in the dye-laser-detector pairings. Due to its broad emission

spectrum, fluorescence from ATTO 490LS can be effectively detected by both detectors. Alexa Fluor 488, however, will also emit with the 488 nm laser pulses and its emitted photons would be collected by the lower bandpass in APD1's dual-BPF indiscriminately from the red-shifted ATTO 490LS-derived photons. ATTO 490LS dye must then be excited by the 488 nm laser and detected with APD2 (675±25 nm BPF). Importantly, the use of the 488 nm laser twice in the scan cycle—first for Alexa Fluor 488 and then for ATTO 490LS—means that these two fluorophores will be at higher risk for photobleaching, for both will progress through excited energy states more often. This risk can be mitigated by changes in labeling densities (i.e. higher density labeling requires less excitation light) as well as optimization of scan times.

DYE CONJUGATION PROTOCOL

As ATTO 490LS, like most other LSS dyes, is not available already conjugated to IgG subclass-specific secondary antibodies, it was necessary to perform this reaction and purification on site. Various options exist for crosslinking small molecules to proteins, with differences in price, reaction size, and reactivity/compatibility. *N*-hydroxysuccinimide (NHS) ester-activated conjugation was chosen for this project due to the availability of reagents (i.e. organic dyes like ATTO 490LS are commonly sold as NHS esters), suitable reaction size (milligram quantities), and compatibility with the ATTO dye chemistry. In this base-catalyzed reaction, nucleophilic primary amines from the protein reagent, here IgG molecules, attack the carbonyl carbon of the NHS ester dye to form a highly stable amide bond with the dye upon loss of the NHS leaving group. This reaction mechanism and its primary intermediate are depicted in **Figure 5**.

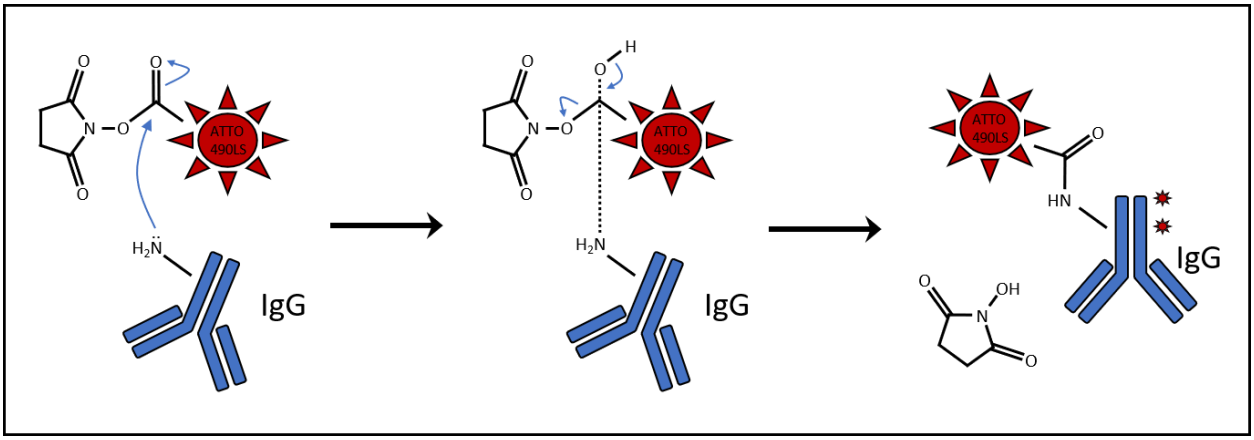

Figure 5. NHS ester-functionalized dye conjugation with immunoglobulins. Amide bonds between functionalized dye molecules (here ATTO 490LS) and free primary amines on the immunoglobulin upon nucleophilic acyl substitution of the NHS leaving group. Multiple dye molecules crosslink with each antibody molecule.

For this study, cross-adsorbed goat anti-mouse IgG1 (1 mg/ml in PBS with no additives) was brought to pH 8.5 with 1 M $NaHCO_3$. ATTO 490LS dye (10 mg/ml in DMSO) was added in 20-fold molar excess to the IgG1 solution and incubated for 2 hours in the dark. 1.5 M NH_2OH was then added to the mixture (1:50 ratio) to quench the reaction. Subsequently, the dye-IgG1 conjugates were purified by column purification through Sephadex G-25 in PD-10 desalting columns according to the manufacturer's instructions. The purification produces two bands of colored eluate: the first colored eluate is the dye conjugated IgG1, and the later eluate is remaining free dye. The fraction containing dye conjugated IgG1 was retained and impurities in the solution, mostly large protein-dye aggregates, removed by ultracentrifugation at 4°C at maximum speed for 10 minutes. The supernatant was then collected, and the ultracentrifugation repeated two more times. Lastly, IgG1 concentration and labeling density were estimated coarsely via UV-vis spectroscopy with a NanoDrop spectrophotometer.

IMAGE ANALYSIS

Resolution improvements were quantified from images with a custom MATLAB script. According to standard practice (Tortarelo *et al*, 2018), full width half maximum (FWHM) measurements from normalized line intensity profiles were calculated as a measurement of image resolution.

MATLAB's curve fitting toolbox was implemented to fit these intensity profiles to a Gaussian model, and the parameters of the curve were then used to determine the FWHM of the model.

RESULTS

STAINING PROTOCOL OPTIMIZATION

A number of parameters were optimized in the development of the following protocol, the most important of which included the (1) fixation reagent; (2) blocking reagent and incubation time; (3) primary and secondary antibody dilutions and incubation times; and (4) mountant.

Two fixation agents were evaluated, methanol and paraformaldehyde (PFA). For the former, cover slips were washed one time with warm PBS, immersed in methanol and cooled to -20°C for 20 seconds, washed two times in PBS to remove residual solvent, and transferred to 4°C for storage. For the latter, cover slips were washed once with warm PBS, immersed in prewarmed (37°C) 4 % PFA for 10 minutes, washed twice to remove residual fixing agent, and transferred to 4°C for storage. Methanol led to widespread disruption of cytoskeletal integrity, while 4% PFA at 37°C led to no noticeable aberrations. In order to avoid disturbing other proteins, PFA fixation was chosen as preferable method and was applied for all subsequent experiments.

Two blocking reagents were used at varying concentrations: purified bovine serum albumin (BSA) and normal goat serum (NGS), both with 100 mM glycine included to quench potential autofluorescence from residual fixation reagent. Whereas 5% BSA provided sufficient blocking in most cases, 100% NGS was found to be the most effective reagent in minimizing background non-specific binding from the phospho-specific GluA2 antibody. 100 mM glycine can also be considered optional depending on sample and fixative type, as no noticeable changes were observed with these samples and fixation protocol.

Primary antibodies were all tested at 1:20, 1:50, 1:100, and 1:200 dilutions in 100% NGS blocking reagent. All were found to operate reliably at 1:100 dilutions, though PSD-93, PSD-95, and Munc-13 antibodies were found to perform well at 1:200 dilutions as well, and all GluA2 antibodies were found to function well at 1:500 dilutions for most samples. The phosphotyrosine-specific GluA2 antibody (Y869/873/876) presented a unique challenge in that it binds non-specifically to poly-D-lysine, the coverslip coating agent used in the primary neuronal culture preparations. Though not performed in this study, it may be advisable to pre-incubate this antibody with poly-

D-lysine coated coverslips to remove non-specific immunoglobulins. This, however, could also lead to significant loss of reactive antibodies, so it should be tested cautiously before application. Secondary antibodies were tested in 1:100, 1:200, 1:500, and 1:1000 dilutions in blocking reagent. Though 1:200 dilutions were used in this study, 1:500 dilutions also provided sufficient signal for STED imaging.

Lastly, two different mountants were tested: ProLong™ Diamond and ProLong™ Glass Antifade Mountants. Both mountants use the same antifade reagent, which performs excellently in STED imaging. ProLong™ Glass, however, offers the advantage of a refractive index of 1.52 after curing, i.e. identical to that of glass coverslips. This reduces aberrations due to refractive index mismatch between sample and coverslip, which is clearly advantageous in super-resolution imaging, where small aberrations in imaging are more noticeable. ProLong™ Diamond, in contrast, cures to a 1.47 refractive index. ProLong™ Glass was chosen for this study, with one caveat for applicability to other systems. Autofocus technology, which is advantageous in long duration and/or multi-stack acquisitions, relies on detection of the refractive index mismatch between the sample and coverslip by an infrared laser. This can thus not be used concomitantly with ProLong™ Glass Antifade, such that the relative advantages for each must be weighed when designing an experiment. The STEDYCON system used in this protocol did not have autofocus functionality, so the Glass Antifade reagent was preferable for its reduction in optical aberrations.

IMAGING OPTIMIZATION

Long Stokes shift dyes, ATTO 490LS included, tend to have particularly broad excitation and emission profiles (cf. ATTO 490LS's profiles in **Figure 4**). This photophysical property carries multiple implications for imaging. First, the excitation laser and emission filters overlap with a smaller percentage of the total spectra of these dyes, resulting less efficient excitation and a smaller fraction of total emitted photons collected. Higher excitation laser power and/or longer dwell times can be employed during acquisition to counteract the dimness of the dyes, though resultant photobleaching provides a fundamental limit to the success of these strategies. Secondly, the broad excitation and emission profiles present challenges for crosstalk between channels. The best strategy to minimize the effects of this crosstalk is to excite the long Stokes

shift fluorophore with a short a wavelength and detect its emission through an emission filter as far removed from this excitation laser as possible, i.e. to maximize the difference between wavelengths used for excitation and emission. This minimizes the likelihood that a shorter Stokes shift dye excited by the laser will be detected in the same channel.

The detector gating system in the STEDYCON provides another means by which these issues of signal collection and crosstalk from ATTO 490LS channels can be avoided. As indicated above (cf. discussion on p.12), gated STED involves the use of pulsed lasers and gated detectors to maximize the depletion effect of the STED beam, thereby maximizing resolution and signal-to-noise ratio. In gated STED, the STED laser is activated immediately after a short excitation pulse (**Figure 3B**), following which the corresponding detector opens for a few nanoseconds. This delay between excitation pulse and detection lowers the likelihood that photons are collected from timepoints when the STED laser was not active, as the detector is not open when these photons would be emitted. This imaging paradigm relies on the kinetics of fluorophore photophysics, which describe a probability distribution of time periods after excitation when a photon will be emitted and detected, i.e. the fluorescence lifetime. After photon absorption, both the spontaneous emission of a photon and stimulated emission driven by the STED beam are probabilistic processes, with the likelihood of depletion increasing with the STED laser's power. However, it is less likely that fluorophores that emitted photons shortly (< 1 ns) after excitation were subject to the STED beam should it have been present at their location These photons are thus considered lower resolution noise, and their removal by gating improves SNR and resolution.

The trade-off with gated detection is the loss of a large number of desired photons along with the noise. As fluorescence lifetime follows an exponential decay distribution, photons are more likely to be released sooner rather than later after excitation. Consequently, a significant portion of the fluorescence signal is lost in the gating process. Thus, the gating parameterization in STED imaging involves a balancing act between signal intensity and resolution/noise.

Three features of ATTO 490 LS make gating particularly relevant: (1) it typically suffers from low signal due to its broad excitation and emission spectra; (2) like other LSS dyes, it has a relatively long fluorescence lifetime (~2.6 ns); and (3) it has a lower STED depletion efficiency than other

commonly used STED dyes. Due to its longer fluorescence lifetime, a longer gate delay is preferable to reduce low resolution noise, further decreasing its already low signal intensity levels. In addition, higher STED powers are required to achieve similar resolution improvements to other dyes, which also effectively reduces the final signal intensity.

To test the optimal gating conditions for ATTO 490LS, four different gating delays—0.5, 1, 1.5 and 2 ns—were tested with a long gate width (8 ns). In this test, 1 ns was found to be the optimal gate delay to collect as much specific signal as possible. Then, four different gate widths—2, 4, 6, and 8 ns—were tested, of which 4 ns performed the best, as the vast majority of ATTO 490LS molecules should have emitted fluorophores by this point, such that any signal collected after the gate is more likely attributable to crosstalk from the other fluorophores, whose fluorescence lifetimes were longer (i.e. Alexa Fluor 594 and Abberior STAR RED also display remarkably long fluorescence lifetimes given their shorter Stokes shifts).

Lastly, the photobleaching effects and mechanical stability of the setup were both evaluated via sequential *z*-stack acquisitions. It was determined that about eight planes could be imaged sequentially with minimal photobleaching when operating with the illumination parameters listed below (**Table 3**). For STED images of the sizes displayed in **Figures 6-10**, the lateral drift of the system over time was low enough to capture the images across a period of about 30 minutes without issue. However, 3D stacks could be even better visualized with use of an alignment algorithm, e.g. for maximum intensity projections or later deconvolution.

FINALIZED PROTOCOLS

A – SAMPLE PREPARATION AND IMMUNOSTAINING

Dissociated primary cortical cultures were prepared as previously described (Hwang *et al.*, 2018). Briefly, cortical tissue from newborn C57BL/6 pups was digested with papain for 20 minutes at 37°C and triturated gently until dissociated. Cells were then plated onto 12 mm round coverslips coated with poly-D-lysine in neurobasal media (Invitrogen) media with B27 (Invitrogen)

supplementation. 5-fluoro-2-deoxyuridine was included in growth media from DIV4 on to discourage glial cell growth.

Samples were fixed at DIV12-14 with 4% paraformaldehyde (PFA) in phosphate buffered saline (PBS; pH 7.4) for 10 minutes at 37°C. Following fixation, samples were stored in PBS at 4°C for up to two weeks prior to immunostaining.

For staining, samples were first permeabilized for 5 minutes in 0.5% Triton X-100 in PBS (pH 7.4), blocked in 100% normal goat serum (NGS) for 10 minutes, and incubated in primary antibodies diluted in 100% NGS for 1 hour at room temperature (RT). Primary antibodies and dilutions included: PSD-93 (N18/30, Neuromab, 1:100), PSD-95 (K28/43, Neuromab, 1:100), GluA2 (Alomone Labs, 1:500), phospho-GluA2 Y869/873/876 (Cell Signaling, 1:500), and Munc-13-1 (Synaptic Systems, 1:200). Following primary antibody incubation, samples were washed five times in PBS, blocked at RT in 100% NGS, and incubated at RT for 1 h in secondary antibodies diluted in 100% NGS. Secondary antibodies and dilutions used included: Abberior STAR RED conjugated goat anti-rabbit IgG (Abberior, 1:200); Alexa Fluor 594 conjugated goat anti-mouse IgG, Fcγ subclass 2a specific (Jackson Immunoresearch, 1:200); Alexa Fluor 488 conjugated goat anti-guinea pig IgG H&L (abcam, 1:200); and ATTO 490LS conjugated goat anti-mouse IgG, Fcγ subclass 1 specific (Thermofisher/Life Technologies, 1:50), prepared as specified in **Methods**. Samples were washed five times in PBS following secondary antibody incubation and embedded with ProLong™ Glass Antifade Mountant (ThermoFisher). After curing, microscope slides were stored in the dark at 4°C.

B – STED IMAGE ACQUISITION

Imaging Parameters		
Pixel size		15 nm
Axial steps (in 3D acquisitions)		250 nm
Pixel dwell time		10 µs
Line Accumulations		8 – 10
LSS	Excitation Power (488 nm)	60 – 80%
	STED Power	60 – 95%
	Gate Delay	1 ns
	Gate Width	3 ns
Alexa Fluor 594	Excitation Power (595 nm)	50 – 75%
	STED Power	65 – 75%
	Gate Delay	1 ns
	Gate Width	7 ns
Abberior STAR RED	Excitation Power (640 nm)	20 – 25%
	STED Power	20 – 45%
	Gate Delay	1 ns
	Gate Width	7 ns

Table 3. Imaging Parameters. Relevant parameters for 4-color STED image acquisitions with the STEDYCON system.

Laser intensities listed in **Table 3** as percentages likely do not translate to other systems, so they are provided as rough estimates of the total power required. Note, too, that the 595 nm laser in this system was slightly uncoupled from its fiberoptic path between the STEDYCON laser and scanning modules, such that the intensities used with this laser are slightly exaggerated.

Prior to image acquisition, it is thus recommended that the user calibrate excitation laser powers with the following guiding criteria. First, the red and far red STED channels should be optimized without the LSS channel. Typical target photon counts in these channels should be 100-200 photons/pixel in the confocal channel and 10-40 photons/pixel in the STED channel. The excitation and STED laser powers that achieve these values will also likely yield the best resolutions. After this, the LSS channel laser should be similarly calibrated. As indicated in *Methods*, the LSS channel will require significantly more laser power to achieve sufficient signal. Care should be taken that the laser is not adjusted so high that the red fluorophore is excited and

emits during LSS acquisition. In light of this, it is likely that lower photon counts will be possible in the LSS channel, though this can be somewhat offset with higher line accumulations. Lastly, the fourth confocal reference channel can be adjusted upward until sufficient signal is achieved.

PROTOCOL DEMONSTRATION

A simplified variation of the protocol described above was first applied to (1) test the capabilities of the STEDYCON system, (2) establish a baseline expectation of achievable resolution in the red and far-red channels, and (3) confirm that protein distributions and morphologies match previous super-resolution studies. Green and long Stokes shift channels were thus omitted, and only two antibodies from different species were used in each immunofluorescent stain. Each primary antibody was tested at least once with Alexa Fluor 594 or Abberior STAR RED.

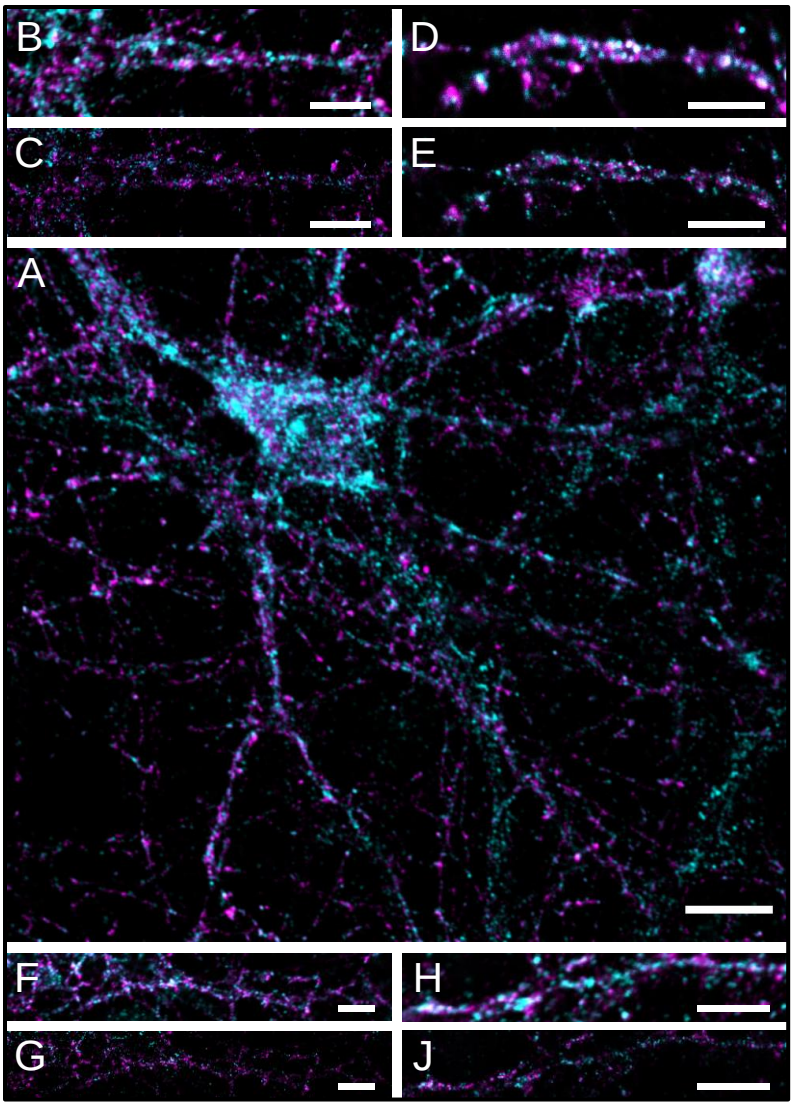

Figure 6. PSD-93 and total GluA2 STED imaging. Representative image of a DIV13 cortical neuron co-stained for PSD-93 (magenta) and total GluA2 (cyan). **A** Confocal overview of a primary cortical neuron (scale bar: 10 µm) **B, D, and F** High-resolution confocal images of individual dendritic branches **C, E, and G** Corresponding STED super-resolution images of dendritic branch insets (scale bars: 4 µm)

Two representative cortical neurons from these experiments can be found in **Figures 6** and **7**. Each stain includes an antibody targeting a structural protein in the red channel and a GluA2-targeting label in the far-red channel. PSD-93 and GluA2 receptors are labeled in **Figure 6**, and PSD-95 and phosphotyrosine (Y869/873/876)-GluA2 are labeled in **Figure 7**. STED imaging was performed on portions of individual dendritic branches, as visualized in **Figures 6B/E/G/I** and

7B/E/G. All four channels show multifold spatial resolution improvements comparable to those expected from advanced full-size STED imaging setups.

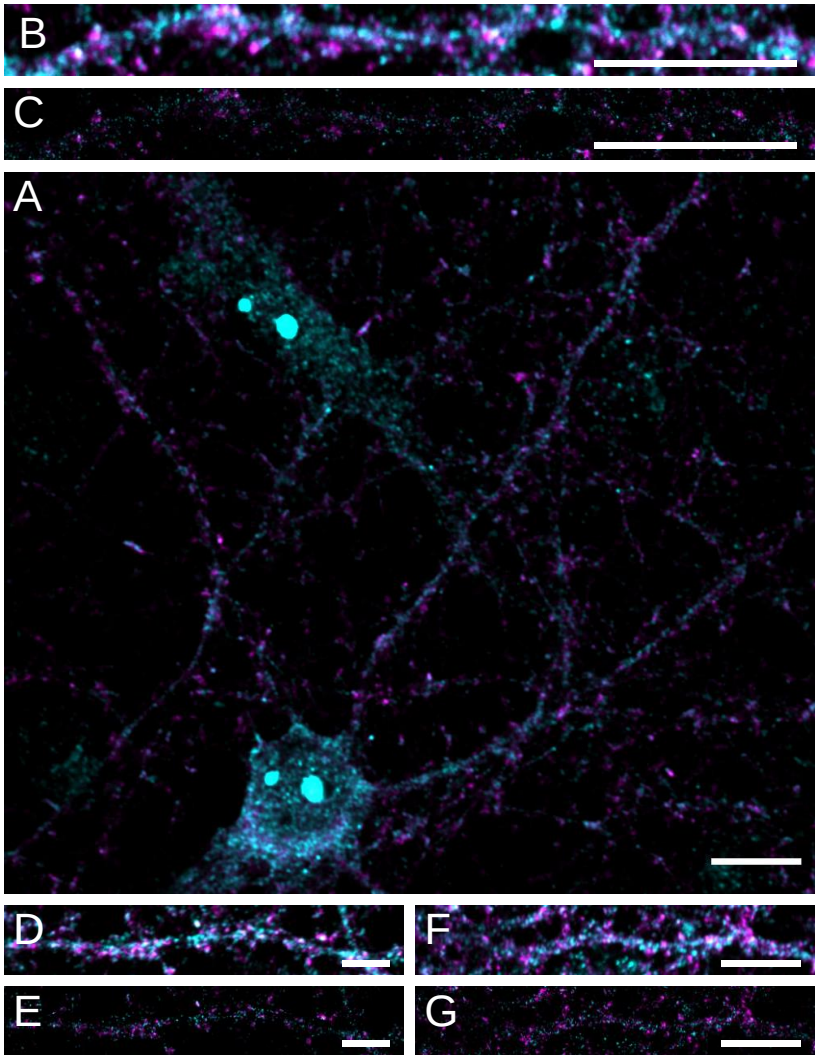

Figure 7. PSD-95 and phosphorylated GluA2 (Y869/873/876) STED imaging. Representative image of a DIV13 cortical neuron co-stained for PSD-95 (magenta) and pY-GluA2 (cyan). **A** Confocal overview of a primary cortical neuron and neighboring glial cell (scale bar: 10 µm) **B, D, and F** High-resolution confocal images of individual dendritic branches **C, E, and G** Corresponding STED super-resolution images of dendritic branch insets (scale bars: 5 µm)

As observable in **Figures** 6 and **7**, STED imaging of PSD-93 and PSD-95 reveals their organization into clumped structures on dendritic spines. This agrees with their roles as

postsynaptic scaffolding proteins and reproduces previous findings *in vitro* and *in vivo* (reviewed in Won *et al.*, 2017). Both total GluA2 (**Figure 6**, cyan) and tyrosine phosphorylated GluA2 (**Figure 7**, cyan), in contrast, are distributed more widely throughout the dendrite and organize into smaller puncta clearly composed of fewer molecules than PSD-93 or PSD-95 scaffolds. In general, the scaffolding proteins exhibit significant spatial overlap at synapses with GluA2 receptors.

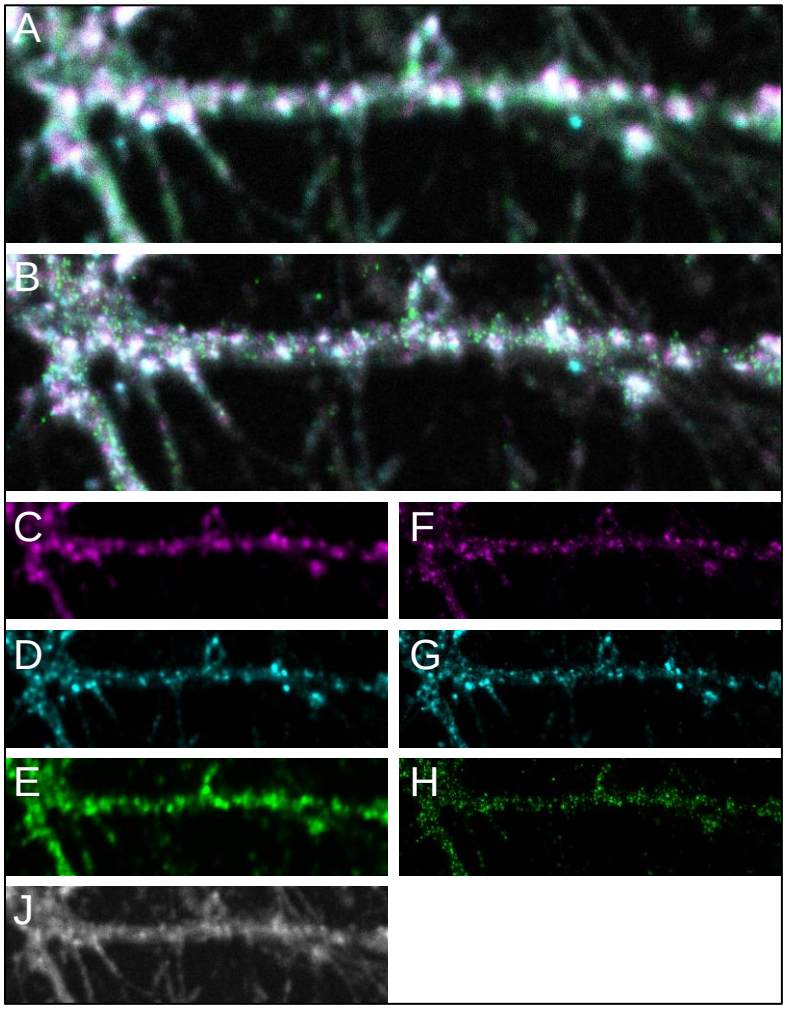

Figure 8. Dendritic Branch in 3 Color STED. Representative image of dendritic branch with four labels, three of which were imaged at STED resolution. Confocal (**A**) and STED (**B**) overlay images of the same dendritic branch. PSD-93 in magenta, PSD-95 in cyan, pY-GluA2 in green, and Munc-13 in grayscale. **C, D, E, J** Individual channels from **A** separated for comparison. **F, G, H** STED channels from **B**, separated for comparison.

Figures 8 and 9 both depict representative dendritic branches from 3 color STED images. In both images, PSD-93 was imaged in the LSS channel, PSD-95 was imaged in the red channel, and pY-GluA2 was imaged in the far-red. Following STED image acquisition, a confocal image of the green channel, where Munc-13 was labeled as a presynaptic marker; this channel is depicted in grayscale in these figures. The 3 color STED images demonstrate the significant extent of spatial overlap in PSD-93 and PSD-95 localization patterns, as could be inferred from their physical interactions in the postsynaptic density (Kim *et al*., 1996). Unfortunately, the Munc-13 stain in these images suffers from extensive non-specific binding, such that its typical location, i.e. exclusively at the presynaptic active zone, is not completely clear. Further work would benefit from optimization of this specific stain or search for an alternative presynaptic label.

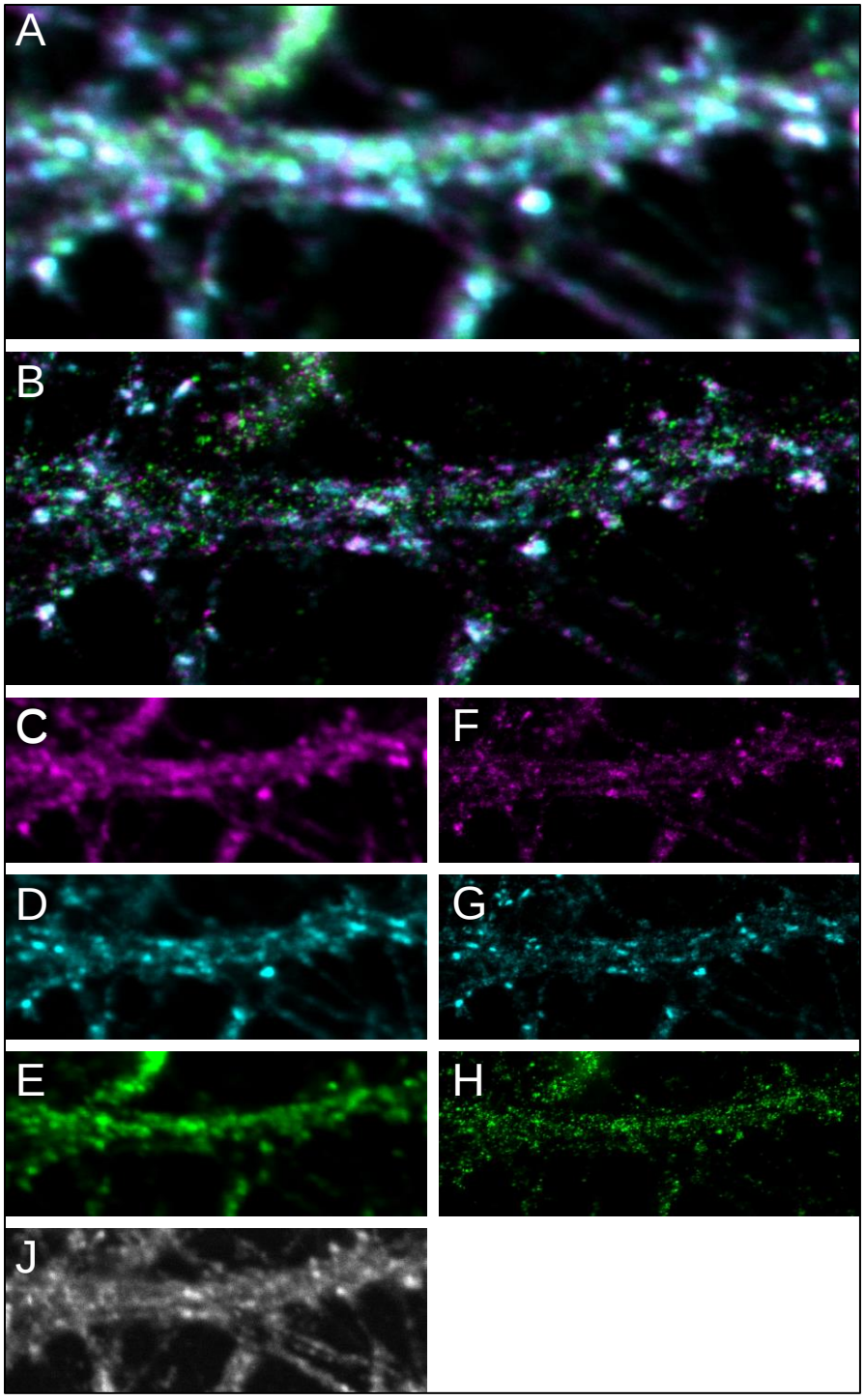

Figure 9. Dendritic Branch in 3 Color STED. Representative image of dendritic branch with four labels, three of which were imaged at STED resolution. Confocal (**A**) and STED (**B**) overlay images of the same dendritic branch. PSD-93 in magenta, PSD-95 in cyan, pY-GluA2 in green, and Munc-13 in grayscale. Munc-13 omitted from STED overlay due to drift between acquisitions. **C, D, E, J** Individual channels from **A** separated for comparison. **F, G, H** STED channels from **B**, separated for comparison.

To quantify the spatial resolutions achieved in this protocol, a custom Matlab script was generated to calculate the full width half maximum (FWHM) value for line intensity profiles. As indicated in **Figure 10**, STED imaging with the methods described above resulted in up to four-fold improvements in the spatial resolution of the imaging system. Though lack of dye-bound fluorescent beads precluded an absolute measurement of spatial resolution in this study, line intensity profiles drawn across the smallest identifiable objects in raw images provided at least a comparison of the microscope's capabilities with and without the STED laser.

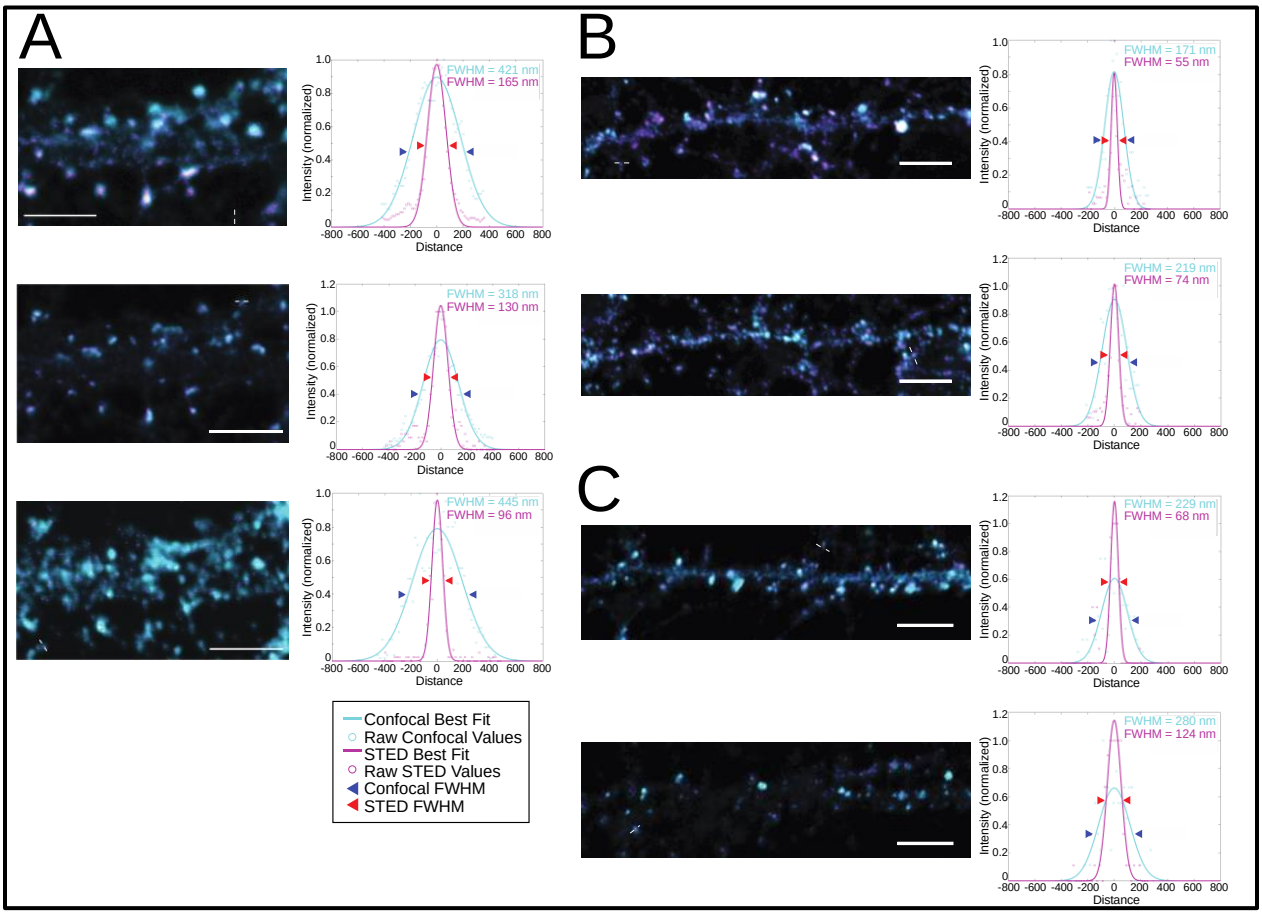

Figure 10. Quantification of Spatial Resolution Improvement. The spatial resolution achieved by the imaging system with this protocol was quantified by fitting line intensity profiles from raw data to a Gaussian. The full width at half maximum (FWHM) was then calculated from the fitting parameters as an estimate of the resolution. Confocal and STED resolutions are visualized for **(A)** 3 color STED imaging of PSD-93, PSD-95, and pY-GluA2; **(B)** two color STED imaging of PSD-93 and total GluA2; and **(C)** two color STED imaging of PSD-95 and pY-GluA2 (Y869/873/876).

CONCLUSION

The protocol described herein provides a ready departure point for detailed analyses of subsynaptic architecture using STED microscopy, even for the novice SR microscopist. Through use of the long Stokes shift dye ATTO 490LS, three color channels were imaged at STED resolution and a fourth as a confocal reference. A four-color staining protocol labeling PSD-93, PSD-95, Munc13-1, and tyrosine-phosphorylated (Y869/873/876) or total GluA2 was implemented in primary cortical neuronal cultures. Up to four-fold improvements in FWHM measurements of spatial resolution were demonstrated, establishing this staining and imaging protocol as a robust method to characterize and construct models of the relative spatial arrangements of synaptic proteins. Moreover, the use of a simplified STED design with only one depletion laser to acquire images indicates that the protocol should suit most, if not all, commercial STED systems.

A primary limitation to this project's results was the suboptimal detector line for red and green emission channels. Due to a dual-BPF design, the green dye Alexa Fluor 488 was detected through a filter that also permitted light in the 617.5±7.5 nm range. The LSS dye, however, is simultaneously excited by the 485 nm laser, and its emission spectra extends into the region allowed by this filter. Thus, it is possible that the LSS dye contributed to the signal of the confocal reference. Accordingly, in this protocol, higher concentrations of green dye were used for staining, such that the confocal reference channel would require very little excitation. A more elegant solution to this problem would be the use of a linear unmixing algorithm, which uses known detector and spectral properties to reassign signals to their appropriate channels for crosstalk correction. This limitation, however, could also be viewed positively: this restrictive design is seldom used in commercial microscopes, and the protocol succeeded despite its presence. Indeed, STEDYCON models with the dual-BPF are no longer available, and all new models contain dedicated detectors for each spectral window.

Another limitation in this study was the use of primary cortical cultures as opposed to fixed tissue specimens. It is possible that cell culture models do not mature and develop synapses similarly to neurons in living brains, such that the same study performed in tissue slices may reveal entirely different morphologies of these synaptic proteins. For this reason, caution is advised when observing the results of this study beyond their use as proof of principle for the protocol.

Further technical elaborations on this method would be dependent on equipment availability. Given the limitations in lasers and detectors with the STEDYCON used in this project, it is unlikely that any further labels could be imaged simultaneously with those already included. New generations of this microscope, as well as models from other companies, include up to four pulsed lasers and four corresponding detectors. With such a system, it would theoretically be possible to achieve four-color STED imaging with a single depletion laser by way of an added shorter wavelength LSS dye (Sidenstein *et al*., 2016). However, such a design could also suffer

from excessive crosstalk between STED channels due to broad LSS dye emission peaks; addition of confocal reference channels, as employed in this project, would be even more difficult.

Lastly, a promising future biological application of this protocol would be its application to fixed tissue preparations from behavioral and genetic studies. For example, tissue prepared from the visual cortex of mice with and without visual experience could reveal experience-dependent maturation or modification of subsynaptic architecture. Likewise, genetic deletion of MAGUK proteins or editing of GluA2 to include phosphomimetic sequences may alter GluA2 receptor complex compositions or its association with scaffolding proteins. These possibilities, and many others, are readily available to even novice STED microscopists with the protocol described here, opening up many promising avenues of research into synaptic nanostructure and its influences on synaptic function and plasticity.

REFERENCES

Abbe, E. Beiträge zur Theorie des Mikroskops und der mikroskopischen Wahrnehmung. *Archiv. Mikrosk. Anat.* 9, 413–418 (1873).

Adesnik, H., & Nicoll, R.A. Conservation of glutamate receptor 2-containing AMPA receptors during long-term potentiation. *J. Neurosci.* 27, 4598-4602 (2007).

Albrecht, D., Winterflood, C. M., Sadeghi, M., Tschager, T., Noé, F., & Ewers, H. Nanoscopic compartmentalization of membrane protein motion at the axon initial segment. *J. Cell Biol.* 215, 37–46 (2016).

Ancona-Esselman S. G., Díaz-Alonso, J., Levy, J. M., Bemben, M. A., & Nicoll, R. A. Synaptic homeostasis requires the membrane-proximal carboxy tail of GluA2. *Proc. Natl. Acad. Sci. U.S.A.* 114, 13266-71 (2017).

Balzarotti, F., Eilers, Y., Gwosch, K. C., Gynnå, A. H., Westphal, V., Stefani, F. D., Elf, J., & Hell, S. W. Nanometer resolution imaging and tracking of fluorescent molecules with minimal photon fluxes. *Science* 355, 606–612 (2016).

Bär, J., Kobler, O., van Bommel, B., & Mikhaylova, M. Periodic F-actin structures shape the neck of dendritic spines. *Sci. Rep*. 6, 37136 (2016).

Bates, M., Huang, B., Dempsey, G. T., & Zhuang, X. Multicolor super-resolution imaging with photo-switchable fluorescent probes. *Science* 317, 1749–1753 (2007).

Betzig, E., Patterson, G. H., Sourgrat, R., Lindwasser, O. W., Olenych, S., Bonifacino, J. S., Davidson, M. W., Lippincott-Schwartz, J., & Hess, H. F. Imaging intracellular fluorescent proteins at nanometer resolution. Science 313, 1642–1645 (2006).

Böhme, M. A., McCarthy, A. W., Grasskamp, A. T., Beuschel, C. B., Goel, P., Jusyte, M., Laber, D., Huang, S., Rey, U., Petzoldt, A. G., Lehmann, M., Göttfert, F., Haghighi, P., Hell, S. W., Owald, D., Dickman, D., Sigrist, S. J., & Walter, A. M. Rapid active zone remodeling consolidates presynaptic potentiation. *Nat. Commun.* 10, 1085 (2019).

Bosch, M., Castro, J., Saneyoshi, T., Matsun, H., Sur, M., & Hayashi, Y. Structural and Molecular Remodeling of Dendritic Spine Substructures during Long-Term Potentiation. Neuron 82, 444-59 (2014).

Broadhead, M. J., Horrocks, M. H., Zhu, F., Muresan, L., Benadvides-Piccione, R., DeFelipe, J., Fricker, D., Kopanitsa, M. V., Duncan, R. R., Klenerman, D., Komiyama, N., Lee, S. F., & Grant, S. G. N. PSD95 nanoclusters are postsynaptic building blocks in hippocampus circuits. *Sci. Rep.* 6, 24626 (2016).

Butkevich, A., Lukinavičius, G., D'Este, E., & Hell, S. W. Cell-Permeant Large Stokes Shift Dyes for Transfection-Free Multicolor Nanoscopy. *J. Am. Chem. Soc.* 139, 12378-81 (2017).

Chazeau, A., Mehidi, A., Nair, D., Gautier, J. J., Leduc, C., Chamma, I., Kage, F., Kechkar, A., Thoumine, O., Rottner, K., Choquet, D., Gautreau, A., Sibarita, J., & Giannone, G. Nanoscale segregation of actin nucleation and elongation factors determines dendritic spine protrusion. *EMBO J.* 33, 2745-64 (2014).

Chen, B. S., Gray, J. A., Sanz-Clemente, A., Wei, Z., Thomas, E. V., Nicoll, R. A., & Roche, K. W. SAP102 mediates synaptic clearance of NMDA receptors. *Cell Rep.* 2, 1120-1128 (2012).

Chen, X., Levy, J.M., Hou, A., Winters, C., Azzam, R., Sousa, A. A., Leapman, R. D., Nicoll, R. A., & T. S. Reese. PSD-95 family MAGUKs are essential for anchoring AMPA and NMDA receptor complexes at the postsynaptic density. *Proc. Natl. Acad. Sci. USA* 112, E6983-E6992 (2015).

Chen, X., Nelson, C.D., Li, X., Winters, C. A., Azzam, R., Sousa, A.A., Leapman, R. D., Gainer, H., Sheng, M., & Reese T. S. PSD-95 is required to sustain the molecular organization of the postsynaptic density. J. Neurosci. 31, 6329-6338 (2011).

Chung, H. J., Xia, J., Scannevin, R. H., Zhang, X., & Huganir, R. L. Phosphorylation of the AMPA receptor subunit GluR2 differentially regulates its interaction with PDZ domain-containing proteins. *J. Neurosci.* 20, 7258-67 (2000).

Collins, M. O., Husi, H., Yu, L., Brandon, J. M., Anderson, C. N., Blackstock, W. P., Choudhary, J. S., & Grant, S.G. Molecular characterization and comparison of the components and multiprotein complexes in the postsynaptic proteome. J. Neurochem. 97, 16–23 (2006).

Crosby, K. C., Gookin, S. E., Garcia, J. D., Hahm, K. M., Dell'Acqua, M. L., & Smith, K. R. Nanoscale Subsynaptic Domains Underlie the Organization of the Inhibitory Synapse. *Cell Rep.* 26, 3284-97 (2019).

D'Este, E., Kamin, D., Balzarotti, F., & Hell, S. W. Ultrastructural anatomy of nodes of Ranvier in the peripheral nervous system as revealed by STED microscopy. *Proc. Natl. Acad. Sci. USA* 114, E191–E199 (2017).

D'Este, E., Kamin, D., Göttfert, F., El-Hady, A., & Hell, S. W. STED nanoscopy reveals the ubiquity of subcortical cytoskeleton periodicity in living neurons. *Cell Rep.* 10, 1246–1251 (2015).

D'Este, E., Kamin, D., Velte, C., Göttfert, F., Simons, M., & Hell, S. W. Subcortical cytoskeleton periodicity throughout the nervous system. *Sci. Rep.* 6, 22741 (2016).

Dani, A., Huang, B., Bergan, J., Dulac, C. & Zhuang, X. Superresolution imaging of chemical synapses in the brain. *Neuron* 68, 843–856 (2010).

Danzl, J. G., Sidenstein, S. C., Gregor, C., Urban, N. T., Ilgen, P., Jakobs, S., & Hell, S. W. Coordinate-targeted fluorescence nanoscopy with multiple off states. Nat. Photonics 10, 122–128 (2016).

Dickson, R. M., Cubitt, A. B., Tsien, R. Y., & Moerner, W. E. On/off blinking and switching behaviour of single molecules of green fluorescent protein. *Nature* 388, 355–358 (1997).

Diering, G. H., & Huganir, R. L. The AMPA Receptor Code of Synaptic Plasticity. *Neuron* 100, 314-29 (2018).

Diering, G. H., Gustina, A. S., & Huganir, R. L. PKA-GluA1 coupling via AKAP5 controls AMPA receptor phosphorylation and cell-surface targeting during bidirectional homeostatic plasticity. *Neuron* 84, 790-805 (2014).

Ehmann, N., van de Linde, S., Alon, A., Ljaschenko, D., Keung, X. Z., Holm, T., Rings, A., DiAntonio, A., Hallermann, S., Ashery, U., Heckmann, M., Sauer, M., & Kittel, R. J. Quantitative super-resolution imaging of Bruchpilot distinguishes active zone states. *Nat. Commun.* 5, 4650 (2014).

Ehmann, N., Sauer, M. & Kittel, R. J. Super-resolution microscopy of the synaptic active zone. *Front. Cell. Neurosci.* 9, 7 (2015).

Einstein, A. Strahlungs-emission und -absorption nach der Quantentheorie. *Verhandlungen der Deutschen Physikalischen Gesellschaft* 18, 318–323 (1916).

Einstein, A. Zur Quantentheorie der Strahlung. *Physikalische Zeitschrift* 18, 121–128 (1917).

Elias, G. M., Funke, L, Stein, V., Grant, S. G., Bredt, D. S., & Nicoll, R.A. Synapse-specific and developmentally regulated targeting of AMPA receptors by a family of MAGUK scaffolding proteins. *Neuron* 52, 307-320 (2006).

Fölling, J., Bossi, M., Bock, H., Medda, R., Wurm, C. A., Hein, B., Jakobs, S., Eggeling, C., & Hell, S. W. Fluorescence nanoscopy by ground-state depletion and single-molecule return. *Nat. Methods* 5, 943–945 (2008).

Fouquet, W. Owald, D., Wichmann, C., Mertel, S., Depner, H., Dyba, M., Hallermann, S., Kittel, R. J., Eimer, S., & Sigrist, S. J. Maturation of active zone assembly by Drosophila Bruchpilot. J. Cell Biol. 186, 129–145 (2009).

Fukata, Y. Dimitrov, A., Boncompain, G., Vielemeyer, O., Perez, F., & Fukata, M. Local palmitoylation cycles define activity-regulated postsynaptic subdomains. J. Cell Biol. 202, 145–161 (2013).

Fulterer, A., Andlauer, T. F. M., Ender, A., Maglione, M., Eyring, K., Woitkuhn, J., Lehmann, M., Matkovic-Rachid, T., Geiger, J. R. P., Walter, A. M., Nagel, K. I., & Sigrist, S. J. Active Zone Scaffold Protein Ratios Tune Functional Diversity across Brain Synapses. Cell Rep. 23, 1259-74 (2018).

Gainey, M. A., Hurvitz-Wolff, J. R., Lambo, M. E., & Turrigiano, G. G. Synaptic scaling requires the GluR2 subunit of the AMPA receptor. *J. Neurosci*. 20, 6479-89 (2009).

Glebov, O. O., Jackson, R. E., Winterflood, C. M., Owen, D. M., Barker, E. A., Doherty, P., Ewers, H., & Burrone, J. Nanoscale Structural Plasticity of the Active Zone Matrix Modulates Presynaptic Function. *Cell Rep.* 18, 2715-28 (2017).

Goebel-Goody, S. M., Baum, M., Paspalas, C. D., Fernandez, S. M., Carty, N. C., Kurup, P., & Lombroso, P. J. Therapeutic implications for striatal-enriched protein tyrosine phosphatase (STEP) in neuropsychiatric disorders. Pharmacol. Rev. 64, 65-87 (2012).

Goel, P., Dufour Bergeron, D., Böhme, M. A., Nunnely, L., Lehmann, M., Buser, C., Walter, A. M., Sigrist, S. J., & Dickman, D. Homeostatic scaling of active zone scaffolds maintains global synaptic strength. *J. Cell Bio.* 218, 1706-24 (2019).

Gustafsson, M. G. L. Nonlinear structured-illumination microscopy: Wide-field fluorescence imaging with theoretically unlimited resolution. *Proc. Natl Acad. Sci. USA* 102, 13081-6 (2005).

Gustafsson, M. G. L. Surpassing the lateral resolution limit by a factor of two using structured illumination microscopy. J. Microsc. 198, 82–87 (2000).

Hayashi, T., & Huganir, R. L. Tyrosine phosphorylation and regulation of the AMPA receptor by SRC family tyrosine kinases. J. Neurosci. 24, 6152-60 (2004).

Hayashi, T., Rumbaugh, G., & Huganir, R. L. Differential regulation of AMPA receptor subunit trafficking by palmitoylation of two distinct sites. Neuron 47, 709-23 (2005).

He, J., Zhou, R., Wu, Z., Carrasco, M. A., Kurshan, P. T., Farley, J. E., Simon, D. J., Wang, G., Han, B., Hao, J., Heller, E., Freeman, M. R., Shen, K., Maniatis, T., Tessier-Lavigne, M., & Zhuang, X. Prevalent presence of periodic actin-spectrin-based membrane skeleton in a broad range of neuronal cell types and animal species. *Proc. Natl. Acad. Sci. U.*S.A. 113, 6029–6034 (2016).

Hell, S. W., & Kroug, M. Ground-state-depletion fluorescence microscopy: A concept for breaking the diffraction resolution limit. *Appl. Phys. B.* 60, 495–497 (1995).

Hell, S. W., & Wichmann, J. Breaking the diffraction resolution limit by stimulated emission: stimulated-emission-depletion fluorescence microscopy. *Opt. Lett.* 19, 780–782 (1994).

Hell, S. W., Microscopy and its focal switch. *Nat. Methods* 6, 24-32 (2009).

Hell, S. W., Sahl, S. J., Bates, M., Zhuang, X., Heintzmann, R., Booth, M. J., Bewersdorf, J., Shtengel, G., Hess, H., Tinnefeld, P., Honigmann, A., Jakobs, S., Testa, I., Cognet, L., Lounis, B., Willig, K. I., Vicidomini, G., Castello, M., Diaspro, A., & Cordes, T. The 2015 super-resolution microscopy roadmap. *J. Phys. D: Appl. Phys.* 48, 1-35 (2015).

Hess, S. T., Girirajan, T. P. K., & Mason, M. D. Ultra-high resolution imaging by fluorescence photoactivation localization microscopy. *Biophys. J.* 91, 4258–4272 (2006).

Hofmann, M., Eggeling, C., Jakobs, S., & Hell, S. W. Breaking the diffraction barrier in fluorescence microscopy at low light intensities by using reversibly photoswitchable proteins. *Proc. Natl Acad. Sci. USA* 102, 17565–17569 (2005).

Hoze, N., Nair, D., Hosy, E., Sieben, C., Manley, S., Herrmann, A., Sibarita, J. B., Choquet, D., & Holcman, D. Heterogeneity of AMPA receptor trafficking and molecular interactions revealed by superresolution analysis of live cell imaging. *Proc. Natl Acad. Sci. USA* 109, 17052–17057 (2012).

Hruska, M., Henderson, N., Le Marchand, S. J., Jafri, H., & Dalva, M. B. Synaptic nanomodules underlie the organization and plasticity of spine synapses. *Nat. Neurosci.* 21, 671-82 (2018).

Irie, M., Hata, Y., Takeuchi, M., Ichtchenko, K., Toyoda, A., Hirao, K., Takai, Y., Rosahl, T. W., & Südhof, T. C. Binding of neuroligins to PSD-95. *Science* 277, 1511–1515 (1997).

Hwang, H., Szucs, M. J., Ding, L. J., Allen, A., Haensgen, H., Gao, F., Andrade, A., Pan, J. Q., Carr, S. A., Ahmad, R., & Xu, W. A schizophrenia risk gene, *NRGN*, bidirectionally modulates synaptic plasticity via regulating the neuronal phosphoproteome. *Biorxiv preprint* (2018).

Kellermayer, B., Ferreira, J. S., Dupuis, J., Levet, F., Grillo-Bosch, D., Linarès-Loyez, J., Bouchet, D., Choquet, D., Rusakov, D. A., Bon, P., Sibarita, J. B., Cognet, L., Sainlos, M., Carvalho, A. L., & Groc, L. Differential Nanoscale Topography and Functional Role of GluN2-NMDA Receptor Subtypes at Glutamatergic Synapses. *Neuron* 100, 106-19 (2018).

Kim, E., Cho, K., Rothschild, A., & Sheng, M. Heteromultimerization and NMDA Receptor-Clustering Activity of Chapsyn-110, a Member of the PSD-95 Family of Proteins. *Neuron* 17, 103-113 (1996).

Kittel, R. J., Wichmann, C., Rasse, T. M., Fouquet, W., Schmidt, M., Schmid, A., Wagh, D. A., Pawlu, C., Kellner, R. R., Willig, K. I., Hell, S. W., Buchner, E., Heckmann, M., & Sigrist, S. J. Bruchpilot promotes active zone assembly, Ca2+ channel clustering, and vesicle release. *Science* 312, 1051–1054 (2006).

Lambert, T. J. FPbase: a community-editable fluorescent protein database. *Nat. Methods* 16, 277–278 (2019).

Lau, C. G. & Zukin, R. S. NMDA receptor trafficking in synaptic plasticity and neuropsychiatric disorders. *Nat. Rev. Neurosci.* 8, 413-426 (2007).

Leite, S. C., Sampaio, P., Sousa, V. F., Nogueira-Rodrigues, J., Pinto-Costa, R., Peters, L. L., Brites, P., & Sousa, M. M. The actin-binding protein α-adducin is required for maintaining axon diameter. *Cell Rep.* 15, 490–498 (2016).

Leterrier, C., Potier, J., Caillol, G., Debamot, C., Rueda Boroni, F., & Dargent, B. Nanoscale architecture of the axon initial segment reveals an organized and robust scaffold. Cell Rep. 13, 2781–2793 (2015).

Levy, J. M., Chen, X., Reese, T. S., & Nicoll, R. A. Synaptic consolidation normalizes AMPAR quantal size following MAGUK loss. Neuron 87, 534-548 (2015).

Liu K.S., Siebert, M., Mertel, S., Knoche, E., Wegener, S., Wichmann, C., Matkovic, T., Muhammad, K., Depner, H., Mettke, C., Bückers, J., Hell, S. W., Müller, M., Davis, G. W., Schmitz, D., & Sigrist, S. J. RIM-binding protein, a central part of the active zone, is essential for neurotransmitter release. *Science* 334, 1565–1569 (2011).

Lukinavicius, G., Reymond, L., D'Este, E., Masharina, A., Göttfert, F., Ta, H., Güther, A., Fournier, M., Rizzo, S., Waldmann, H., Blaukopf, C., Sommer, C., Gerlich, D. W., Amdt, H. D., Hell, S. W., & Johnsson, K. Fluorogenic probes for live-cell imaging of the cytoskeleton. *Nat. Methods* 11, 731–733 (2014).

Lussier, M. P., Sanz-Clemente, A., & Roche, K. W. Dynamic Regulation of N-Methyl-d-aspartate (NMDA) and α-Amino-3-hydroxy-5-methyl-4-isoxazolepropionic Acid (AMPA) Receptors by Posttranslational Modifications. J. Biol. Chem. 290, 28596-28603 (2015).

MacGillavry, H. D., Song, Y., Raghavachari, S. & Blanpied, T. A. Nanoscale scaffolding domains within the postsynaptic density concentrate synaptic AMPA receptors. *Neuron* 78, 615–622 (2013).

Masch, J. M., Steffens, H., Fischer, J., Engelhardt, J., Hubrich, J., Keller-Findeisen, J., D'Este, E., Urban, N. T., Grant, S. G. N., Sahl, S. J., Kamin, D., & Hell, S. W. Robust nanoscopy of a synaptic protein in living mice by organic-fluorophore labeling. *Proc. Natl. Acad. Sci. USA* 21, E8047-56 (2018).

Mayer, M. L., Westbrook, G. L., & Guthrie, P. B. Voltage-dependent block by Mg2+ of NMDA responses in spinal cord neurons. *Nature* 309, 261-3 (1984).

Nägerl, U. V., Willig, K. I., Hein, B., Hell, S. W., & Bonhoeffer, T. Live-cell imaging of dendritic spines by STED microscopy. *Proc. Natl. Acad. Sci. USA* 105, 18982–18987 (2008).

Nair, D., Hosy, E., Petersen, J. D., Constals, A., Giannone, G., Choquet, D., & Sibarita, J. B. Super-resolution imaging reveals that AMPA receptors inside synapses are dynamically organized in nanodomains regulated by PSD95. *J. Neurosci.* 33, 13204–13224 (2013).

Nishimune, H., Badawi, Y., Mori, S. & Shigemoto, K. Dual-color STED microscopy reveals a sandwich structure of Bassoon and Piccolo in active zones of adult and aged mice. *Sci. Rep.* 6, 27935 (2016).

Owald, D., Fouquet, W., Schmidt, M., Wichmann, C., Mertel, S., Depner, H., Christiansen, F., Zube, C., Quentin, C., Körner, J., Urlaub, H., Mechtler, K., & Sigrist, S. J. A Syd-1 homologue regulates pre- and postsynaptic maturation in Drosophila. *J. Cell Biol.* 188, 565–579 (2010).

Paoletti, P., Bellone, C., & Zhou, Q. NMDA receptor subunit diversity: impact on receptor properties, synaptic plasticity and disease. *Nat. Rev. Neurosci.* 14, 383-400 (2013).

Peng, J., Kim, M. J., Cheng, D., Duong, D. M., Gygi, S. P., & Sheng, M. Semi-quantitative proteomic analysis of rat forebrain postsynaptic density fractions by mass spectrometry. *J. Biol. Chem.* 279, 21003–21011 (2004).

Reiner, A., & Levitz, J. Glutamatergic signaling in the central nervous system: Ionotropic and metabotropic receptors in concert. *Neuron* 98, 1080-1098 (2018).

Rust, M. J., Bates, M., & Zhuang, X. Sub-diffraction-limit imaging by stochastic optical reconstruction microscopy (STORM). *Nat. Methods* 3, 793–796 (2006).

Sahl, S. J., Hell, S. W., & Jakobs, S. Fluorescence nanoscopy in cell biology. *Nat. Rev. Mol.* 18, 685-701 (2017).

Sakamoto, H., Ariyoshi, T., Kimpara, N., Sugao, K., Taiko, I., Takikawa, K., Asanuma, D., Namiki, S., & Hirose, K. Synaptic weight set by Munc13-1 supramolecular assemblies. *Nat. Neurosci.* 21, 41-49 (2018).

Schermelleh, L., Ferrand, A., Huser, T., Eggeling, C., Sauer, M., Biehlmaier, O., Drummen, G. P. C. Super-resolution microscopy demystified. Nat. Cell. Bio. 21, 72-84 (2019).

Schwenk, J., Harmel, N., Zolles, G., Bildl, W., Kulik, A., Heimrich, B., Chisaka, O., Jonas, P., Schulte, U., Fakler, B., & Klöcker, N. Functional proteomics identify cornichon proteins as auxiliary subunits of AMPA receptors. *Science* 323, 1313–1319 (2009).

Seabold, G. K., Surette, A., Lim, I. A., Weinberg, R. J., & Hell, J.W. Interaction of the tyrosine kinase Pyk2 with the N-methyl-D-aspartate receptor complex via the Src homology 3 domains of PSD-95 and SAP102. J. Biol. Chem. 278, 15040-15048 (2003).

Sednev, M. V., Belov, V. N., & Hell, S. W. Fluorescent dyes with large Stokes shifts for super-resolution optical microscopy of biological objects: A review. *Methods Appl. Fluores.* 3, [042004] (2015).

Sharonov, A., & Hochstrasser, R. M. Wide-field subdiffraction imaging by accumulated binding of diffusing probes. *Proc. Natl Acad. Sci. USA* 103, 18911–18916 (2006).

Sheng, M., & Kim, E. The Postsynaptic Organization of Synapses. *Cold Spring Harb. Perspect. Biol.* 3, 1-20 (2011).

Sidenstein, S. C., D'Este, E., Böhm, M. J., Danzl, J. G., Belov, V. N., & Hell, S. W. Multicolour multilevel STED nanoscopy of actin/spectrin organization at synapses. Sci. Rep. 6, 26725 (2016).

Sigal, Y. M., Zhou, R., & Zhuang, X. Visualizing and discovering cellular structures with super-resolution microscopy. *Science* 361, 880-7 (2018).

Straub, C., & Tomita, S. The regulation of glutamate receptor trafficking and function by TARPs and other transmembrane auxiliary subunits. *Curr. Opin. Neurobiol.* 3, 488-95 (2012).

Südhof, T. C. Neurotransmitter release: the last millisecond in the life of a synaptic vesicle. Neuron 80, 675–690 (2013).

Südhof, T.C. The presynaptic active zone. *Neuron* 75, 11–25 (2012).

Sydor, A. M., Czymmek, K. J., Puchner, E. M., & Mennella, V. Super-Resolution Microscopy: From Single Molecules to Supramolecular Assemblies. *Trends Cell Bio.* 25, 730-48 (2015).

Takasaki, K., & Sabatini, B. L. Super-resolution 2-photon microscopy reveals that the morphology of each dendritic spine correlates with diffusive but not synaptic properties. Front. Neuroanat. 8, 29 (2014).

Tan, H. L., Queenan, B. N., & Huganir, R. L. GRIP1 is required for homeostatic regulation of AMPAR trafficking. *Proc. Natl. Acad. Sci. U.S.A.* 112, 10026-31 (2015).

Tang, A. H., Chen, H., Li, T. P., Metzbower, S. R., MacGillavry, H. D., & Blanpied, T. A. A trans-synaptic nanocolumn aligns neurotransmitter release to receptors. *Nature* 536, 210–214 (2016).

Tatavarty, V., Sun, Q., & Turrigiano, G. G. How to Scale Down Postsynaptic Strength. *J. Neurosci.* 33, 13179-89 (2013).

Taylor, E. W., Wang, K., Nelson, A. R., Bredemann, T. M., Fraser, K. B., Clinton, S. M., Puckett, R., Marchase, R. B., Chatham, J. C., & McMahon, L. L. O-GlcNAcylation of AMPA Receptor GluA2 Is Associated with a Novel Form of Long-Term Depression at Hippocampal Synapses. *J. Neurosci.* 34, 10-21 (2014).

Testa, I., Urban, N. T., Jakobs, S., Eggeling, C., Willig, K. I., & Hell, S. W. Nanoscopy of living brain slices with low light levels. Neuron 75, 992-1000 (2012).

Tezuka, T., Umemori, H., Akiyama, T., Nakanishi, S., & Yamamoto, T. PSD-95 promotes Fyn-mediated tyrosine phosphorylation of the N-methyl-D-aspartate receptor subunit NR2A. Proc. Natl. Acad. Sci. U.S.A. 96, 435-440 (1999).

Tomita, S., Chen, L., Kawasaki, Y., Petralia, R. S., Wenthold, R. J., Nicoll, R. A., & Bredt, D. S. (2003) Functional studies and distribution define a family of transmembrane AMPA receptor regulatory proteins. J. Cell. Biol. 161, 805– 816 (2003).

Tonnesen, J., Katona, G., Rozsa, B., & Nägerl, U. V. Spine neck plasticity regulates compartmentalization of synapses. Nat. Neurosci. 17, 678–685 (2014).

Tortarelo, G., Castello, M., Diaspro, A., Koho, S., & Vicidomini, G. Evaluating image resolution in stimulated emission depletion microscopy. *Optica* 5, 32-5 (2018).

Traynelis, S. F., Wollmuth, L. P., McBain, C. J., Menniti, F. S., Vance, K. M., Ogden, K. K., Hansen, K. B., Yuan, H., Myers, S. J., & Dingledine, R. Glutamate receptor ion channels: structure, regulation, and function. Pharmacol. Rev. 62: 405-96 (2010).

Urban, B. E., Xiao, L., Chen, S., Yang, H., Dong, B., Kozorovitskiy, Y., & Zhang, H. F. In Vivo Superresolution Imaging of Neuronal Structure in the Mouse Brain. IEEE Trans. Biomed. Eng. 65, 232-8 (2018).

Vicidomini, G., Bianchini, P., & Diaspro, A. STED super-resolved microscopy. *Nat. Methods* 53, 173-82 (2018).

Wegner, W., Mott, A. C., Grant, S. G. N., Steffens, H., & Willig, K. I. *In vivo* STED microscopy visualizes PSD95 sub-structures and morphological changes over several hours in the mouse visual cortex. *Sci. Rep.* 8, 219 (2018).

Widagdo, J., Chai, Y. J., Ridder, M. C., Chau, Y. Q., Johnson, R. C., Sah, P., Huganir, R. L., & Anggono, V. Activity-Dependent Ubiquitination of GluA1 and GluA2 Regulates AMPA Receptor Intracellular Sorting and Degradation. Cell Rep. 10, 783-95 (2015).

Widagdo, J., Guntupalli, S., Jang, S. E., & Anggono, V. Regulation of AMPA Receptor Trafficking by Protein Ubiquitination. Front. Mol. Neurosci. 10, 347 (2017).

Wilhelm, B.G., Mandad, S., Truckenbrodt, S., Kröhnert, K., Schäfer, C., Rammner, B., Koo, S. J., Claßen, G. A., Krauss, M., Haucke, V., Urlaub, H., Rizzoli, S. O. Composition of isolated synaptic boutons reveals the amounts of vesicle trafficking proteins. *Science* 344, 1023–1028 (2014).

Willig, K. I., Rizzoli, S. O., Westphal, V., Jahn, R., & Hell, S. W. STED microscopy reveals that synaptotagmin remains clustered after synaptic vesicle exocytosis. *Nature* 440, 935–939 (2006).

Won, S., lncontro, S., Nicoll, R. A., & Roche, K. W. PSD-95 stabilizes NMDA receptors by inducing the degradation of STEP61. Proc. Natl. Acad. Sci. U.S.A. 113, E4736-44 (2016).

Won, S., Levy, J. M., Nicoll, R. A., & Roche, K. W. MAGUKs: multifaceted synaptic organizers. *Curr. Opin. Neurobiol.* 43, 94-101 (2017).

Xu, K., Zhong, G., & Zhuang, X. Actin, spectrin, and associated proteins form a periodic cytoskeletal structure in axons. *Science* 339, 452–456 (2013).

Zhong, G., He, J., Zhou, R., Lorenzo, D., Babcock, H. P., Bennett, V., & Zhuang, X. Developmental mechanism of the periodic membrane skeleton in axons. *eLife* 3, e04581 (2014).